

# 000 001 002 003 004 005 006 007 008 009 010 011 012 013 014 015 016 017 018 019 020 021 022 023 024 025 026 027 028 029 030 031 032 033 034 035 036 037 038 039 040 041 042 043 044 045 046 047 048 049 050 051 052 053 NEURAL OPTIMAL TRANSPORT MEETS MULTIVARIATE CONFORMAL PREDICTION

Anonymous authors

Paper under double-blind review

## ABSTRACT

We propose a framework for *vector quantile regression* (VQR) that combines neural optimal transport with amortized optimization, and apply it to multivariate conformal prediction. Classical quantile regression does not extend naturally to multivariate responses, while existing approaches often ignore the geometry of joint distributions. Our method parameterizes the conditional vector quantile function as the gradient of a convex potential implemented by an input-convex neural network, ensuring monotonicity and uniform ranks. To reduce the cost of solving high-dimensional variational problems, we introduce amortized optimization of the dual potentials, yielding efficient training and faster inference.

We then exploit the induced multivariate ranks for conformal prediction, constructing distribution-free predictive regions with finite-sample validity. Unlike coordinatewise methods, our approach adapts to the geometry of the conditional distribution, producing tighter and more informative regions. Experiments on benchmark datasets show improved coverage–efficiency trade-offs compared to baselines, highlighting the benefits of integrating neural optimal transport with conformal prediction.

## 1 INTRODUCTION

Quantile regression has long been a cornerstone for modeling heterogeneous conditional distributions in the univariate setting (Koenker & Bassett, 1978; Koenker, 2005). Estimating conditional quantiles rather than conditional means provides a more complete view of the conditional law of a response variable and has enabled advances in econometrics, statistics, and machine learning. Extending these ideas to multivariate responses, however, remains challenging: unlike the scalar case,  $\mathbb{R}^d$  lacks a natural total ordering, and early multivariate notions of quantiles, based on projections, spatial medians, or depth functions, inherit only part of the desirable scalar properties (Chaudhuri, 1996; Hallin et al., 2021).

Recent progress in optimal transport has offered a principled definition of multivariate ranks and quantiles (Chernozhukov et al., 2017; Hallin & Konen, 2024). By interpreting quantiles as transport maps from a reference distribution to the law of  $Y$ , these approaches recover distribution-free center-outward ranks and quantile regions that extend univariate order statistics to high dimensions. Building on this perspective, vector quantile regression (VQR; Carlier et al., 2016; 2017) introduces conditional vector quantile functions (CVQFs), monotone maps that represent  $Y$  as a transformation of latent uniform variables given covariates. CVQFs provide a rich yet tractable representation of conditional distributions, with promising extensions to nonlinear models (Rosenberg et al., 2023; Vedula et al., 2023b;a; Sun et al., 2022; del Barrio et al., 2025).

In parallel, conformal prediction has emerged as a powerful framework for constructing predictive regions with finite-sample coverage guarantees (Angelopoulos et al., 2023). Although well studied in the univariate case, multivariate extensions are less developed. Existing approaches include coordinate-wise methods that ignore the geometry of joint distributions (Zhou et al., 2024; Diquigiovanni et al., 2021); reductions of the multivariate problem to one dimension via a score (Dheur et al., 2025; Izbicki et al., 2019); and structured approaches that use deep generative embeddings (Dheur et al., 2025; Feldman et al., 2023). Many of these methods rely on heuristics with limited theoretical foundations. For an overview of recent developments in multivariate conformal regression, see (Dheur et al., 2025). Very recent work begins to bridge this gap by incorporating optimal-

054 transport-based multivariate ranks into conformal prediction, yielding theoretically grounded multivariate prediction sets (Thurin et al., 2025; Klein et al., 2025).  
 055  
 056

057 In this paper, we leverage a neural optimal transport framework for learning CVQFs which allows  
 058 us to estimate parametric cyclically monotone vector quantiles and multivariate ranks. Building  
 059 on the resulting multivariate ranks, we use conformal prediction to produce distribution-free valid  
 060 confidence regions that adapt to the geometry of conditional distributions in the multivariate setting.  
 061

062 We make three main contributions:  
 063

- 064 • We introduce a **neural optimal transport framework for vector quantile regression** (VQR), leveraging *input-convex neural networks* to learn continuous vector quantile maps  
 065 and multidimensional ranks (Section 3).
- 066 • We propose the first **principled integration of vector quantiles and multivariate ranks** into **conformal prediction**, yielding *distribution-free predictive regions* that adapt to the  
 067 geometry of conditional distributions (Section 4).
- 068 • We show that the resulting **conformal prediction sets** consistently *outperform coordinate-  
 069 wise and representation-based baselines* across benchmarks, demonstrating both tighter  
 070 coverage and improved calibration (Section 6).  
 071

## 073 2 CONSTRUCTING MULTIVARIATE CONFIDENCE SETS

074 We start by informally introducing the conditional vector quantile and rank maps that aim to provide  
 075 a flexible representation of the conditional law of  $Y$  given  $X$ .  
 076

077 **Quantiles in 1D and Confidence Sets.** Let us first consider the case of  $Y \in \mathcal{Y} \subseteq \mathbb{R}$ . Let  
 078  $(Y, X) \sim F_{YX}$  and let  $F_{Y|X}$  be the conditional distribution of  $Y$  given  $X$ . Then, the quantile  
 079 function  $Q_{Y|X}(\cdot, x)$  for any  $\alpha \in [0, 1]$  outputs the corresponding quantile value  $Q_{Y|X}(\alpha, x) \in \mathcal{Y}$   
 080 of distribution  $F_{Y|X=x}$ . The knowledge of the quantile function is instrumental for the  
 081 construction of the confidence sets. For example, for a given  $\alpha \in (0, 1)$  one can define  $\mathcal{C}_\alpha(x) =$   
 082  $[Q_{Y|X}(\alpha/2, x), Q_{Y|X}(1-\alpha/2, x)]$ . By construction, this confidence set is valid, i.e.  $\mathbb{P}(Y \in \mathcal{C}_\alpha(x) |$   
 083  $X = x) = 1 - \alpha$ .  
 084

085 The inverse map  $Q_{Y|X}^{-1}$  is sometimes called a rank function as for any value of variable  $y$  it pro-  
 086 duces the value on an interval  $Q_{Y|X}^{-1}(y, x) \in [0, 1]$  which can be interpreted as the rank of  $y$   
 087 among its possible values with respect to the distribution  $F_{Y|X=x}$ . Importantly, the distribution  
 088 of  $Q_{Y|X}^{-1}(Y, X) | X = x$  is uniform on  $[0, 1]$ . In its turn, the knowledge of the rank function gives  
 089 an alternative way to define the confidence interval  $\mathcal{C}_\alpha^{\text{pull}}(x) = \{y: Q_{Y|X}^{-1}(y, x) \in [\alpha/2, 1 - \alpha/2]\}$ .  
 090 Obviously,  $\mathcal{C}_\alpha(x)$  and  $\mathcal{C}_\alpha^{\text{pull}}(x)$  coincide. However, their functional forms give alternative views on  
 091 how one can construct the confidence interval depending on having the access to the quantile or to  
 092 the rank function.  
 093

094 **Multivariate Quantiles.** In the absence of a natural order on  $\mathbb{R}^d$  for  $d > 1$ , the definition of  
 095 the multivariate quantile is not trivial. In this paper, we will study the definitions of multivariate  
 096 quantiles based on optimal transport; see among others (Carlier et al., 2016; Hallin et al., 2021;  
 097 Hallin & Konen, 2024). We start by looking at a specific example, while the full exposition in  
 098 Section 3 is given below.  
 099

100 Define  $r_{1-\alpha} \in \mathbb{R}_+$  such that the Euclidean ball  $B(0, r_{1-\alpha}) \subset \mathcal{U} := B(0, 1)$  satisfies the condition  
 101  $\text{Volume}(B(0, r_{1-\alpha})) = 1 - \alpha$ . Then, it can be shown (see Theorem 1 below) that there exists a  
 102 map  $Q_{Y|X}(u, x)$  and a uniform random variable  $U$  over the  $\mathcal{U}$ , independent of  $X$  such that  $Y =$   
 103  $Q_{Y|X}(U, X)$  almost surely. This map is called a *vector quantile*. The corresponding inverse map  
 104  $Q_{Y|X}^{-1}(y, x) \in \mathcal{U}$  becomes a natural analogue of the *rank function*.  
 105

106 We can directly proceed with construction of confidence sets based on  $Q_{Y|X}^{-1}(Y, X)$ . For  $x \in \mathcal{X}$ ,  
 107 define the *pullback set*

$$\mathcal{C}_\alpha^{\text{pb}}(x) := \{y: Q_{Y|X}^{-1}(y, x) \in B(0, r_{1-\alpha})\}. \quad (1)$$

108 Using the properties of quantile and rank functions we get that  
 109  $\mathbb{P}(Y \in \mathcal{C}_\alpha^{\text{pb}}(X)) = \mathbb{P}_{(U,X) \sim F_U \otimes F_X}(\|Q_{Y|X}^{-1}(Q_{Y|X}(U,X), X)\| \leq r_{1-\alpha}) = \mathbb{P}_{U \sim F_U}(\|U\| \leq r_{1-\alpha})$ .  
 110  
 111 Hence, the coverage of the pullback set  $\mathcal{C}_\alpha^{\text{pb}}(x)$  is exactly  $1 - \alpha$  as required.  
 112

113 **Conformalized Confidence Sets.** In practice, we can only have access to the estimator  $\hat{Q}_{Y|X}^{-1}$  of  
 114  $Q_{Y|X}^{-1}$ . One can consider plug-in confidence sets constructed directly from these estimators. How-  
 115 ever, such sets fail to guarantee coverage as generally  $\hat{Q}_{Y|X}^{-1} \neq Q_{Y|X}^{-1}$ . Consequently, the coverage  
 116 of  $\mathcal{C}_\alpha^{\text{pull}}(X)$  may be miscalibrated, motivating the use of conformal prediction. Conformal pre-  
 117 diction corrects such miscalibration, providing finite-sample, distribution-free *marginal* coverage  
 118 guarantees. Specifically, given a calibration set  $\mathcal{D}_{\text{cal}} = \{(X_i, Y_i)\}_{i=1}^n$  independent of the training  
 119 data, consider a score  $S_i = \|\hat{Q}_{Y|X}^{-1}(Y_i, X_i)\|, i = 1, \dots, n$ . Then, split-conformal prediction  
 120 constructs a set  $\hat{\mathcal{C}}_\alpha^{\text{pb}}(X_{\text{test}}) \subseteq \mathcal{Y}$  for a new test point  $(X_{\text{test}}, Y_{\text{test}})$  based on the scores  $\{S_i\}_{i=1}^n$  and  
 121  $S_{\text{test}} = \|\hat{Q}_{Y|X}^{-1}(Y_{\text{test}}, X_{\text{test}})\|$  such that  
 122

$$\mathbb{P}\{Y_{\text{test}} \in \hat{\mathcal{C}}_\alpha^{\text{pb}}(X_{\text{test}})\} \geq 1 - \alpha,$$

123 under the assumption that  $(X_1, Y_1), \dots, (X_n, Y_n), (X_{\text{test}}, Y_{\text{test}})$  are exchangeable (Romano et al.,  
 124 2019; Angelopoulos et al., 2023). The other choices of the score are possible, see discussion in  
 125 Section 4.

126 In what follows, we discuss various approaches to construct  $\hat{Q}_{Y|X}$  and  $\hat{Q}_{Y|X}^{-1}$  based on neural opti-  
 127 mal transport.  
 128

### 3 VECTOR QUANTILE REGRESSION VIA OPTIMAL TRANSPORT

131 We now proceed to recall the mathematical underpinnings of vector quantile regression and  
 132 multidimensional ranks, where we follow closely the formulation of Carlier et al. (2016); Hallin et al.  
 133 (2021). Let  $(Y, X)$  be a random vector on a complete probability space  $(\Omega, \mathcal{A}, \mathbb{P})$ , where  $Y \in \mathbb{R}^{d_y}$   
 134 and  $X \in \mathbb{R}^{d_x}$ . Denote by  $F_{YX}$  the joint law of  $(Y, X)$ , by  $F_{Y|X}$  the conditional law of  $Y$  given  $X$ ,  
 135 and by  $F_X$  the marginal of  $X$ . Let  $U$  be a random vector on  $(\Omega, \mathcal{A}, \mathbb{P})$  with reference distribution  
 136  $F_U$ . We write  $\mathcal{Y}, \mathcal{X}, \mathcal{U}, \mathcal{Y} \times \mathcal{X}, \mathcal{U} \times \mathcal{X}$  for the supports of  $F_Y, F_X, F_U, F_{Y|X}, F_{U|X}$ , and  $\mathcal{Y}_x$  for the  
 137 support of  $F_{Y|X=x}$ . By [U ≤ u for  \$U, u \in \mathbb{R}^d\$  we mean a coordinatewise inequality between the  
 138 vectors, which leads to  \$F\_U\(u\) = F\_U\(u\_1, \dots, u\_d\) = \mathbb{P}\(U\_1 \leq u\_1, \dots, U\_d \leq u\_d\) = \mathbb{P}\(U \leq u\)\$ .](#)  
 139 Norms are Euclidean on  $\mathbb{R}^d$ .  
 140

141 The following basic properties of distributions  $F_U$  and  $F_{Y|X}$  are required for the construction of  
 142 OT-based vector quantiles and rank functions.  
 143

144 **Assumption 1.** *The reference distribution  $F_U$  admits a density  $f_U$  with respect to Lebesgue measure  
 145 on  $\mathbb{R}^d$ , with convex support  $\mathcal{U} \subseteq \mathbb{R}^d$ .*  
 146

147 Typical choices for  $F_U$  include the uniform distribution on  $[0, 1]^d$ , the Gaussian  $\mathcal{N}(0, I_d)$ , or any  
 148 distribution on  $\mathbb{R}^d$  with convex support.  
 149

150 **Assumption 2.** *For each  $x \in \mathcal{X}$ , the conditional law  $F_{Y|X}(\cdot, x)$  has a density  $f_{Y|X}(\cdot, x)$ .*  
 151

152 Our goal is to construct a push-forward of  $U \sim F_U$  to  $Y$  such that the conditional law of  $Y | X$   
 153 equals  $F_{Y|X}$ . In the multivariate setting, monotonicity requires the map to be the gradient of a  
 154 convex function, a natural generalization of scalar monotonicity. This motivates the *conditional  
 155 vector quantile function* (CVQF).

156 **Theorem 1** (Carlier et al. (2016), Theorems 2.1 & 2.2). *Suppose Assumption 1 holds. Then:*  
 157

- (i) *For each  $x \in \mathcal{X}$ , there exists a measurable map  $u \mapsto Q_{Y|X}(u, x)$ , unique  $F_U$ -a.e., which is  
 158 the gradient of a convex function and pushes  $F_U$  forward to  $F_{Y|X=x}$ .*
- (ii) *Consequently, there exists  $U \sim F_U$  such that  $Y = Q_{Y|X}(U, X)$  a.s. with  $U | X \sim F_U$ .*
- (iii) *Additionally, if Assumption 2 holds, then there exists a measurable inverse map  $Q_{Y|X}^{-1}(y, x) \in  
 159 \mathcal{U}$  such that  $Q_{Y|X}^{-1}(Q_{Y|X}(u, x), x) = u$  for  $F_U$ -a.e.  $u$ , and  $\mathbb{P}(Q_{Y|X}^{-1}(Y, X) \leq u | X = x) =  
 160 F_U(u)$ .*

The map  $y \mapsto Q_{Y|X}^{-1}(y, x)$  is the *conditional vector rank*. For  $d = 1$  it coincides with the conditional CDF, but not for  $d > 1$  (Hallin et al., 2021; Hallin & Konen, 2024; del Barrio et al., 2025).

Finally, the following assumption is needed to ensure the efficient computation of  $Q_{Y|X}$  and  $Q_{Y|X}^{-1}$ .

**Assumption 3.**  $Y$  and  $U$  have finite second moments:  $\mathbb{E}[\|Y\|^2] < \infty$  and  $\mathbb{E}[\|U\|^2] < \infty$ .

Under this, the CVQF solves a conditional optimal transport problem:  $\min_V \mathbb{E}[\|Y - V\|^2]$  s.t.  $V \mid X \sim F_U$ , equivalently  $\max_V \mathbb{E}[V^\top Y]$  under the same constraint. The dual program is

$$\min_{\psi, \varphi} \mathbb{E}[\varphi(V, X)] + \mathbb{E}[\psi(Y, X)] \quad \text{s.t.} \quad \varphi(u, x) + \psi(y, x) \geq u^\top y, \quad (2)$$

where  $V$  is any vector such that  $V \mid X \sim F_U$ . The following properties for the solution of (2) can be stated.

**Theorem 2** (Carlier et al. (2016), Theorem 2.3). *Suppose Assumptions 1–3 hold. Then,*

(i) *There exist potentials  $\varphi(u, x)$  and  $\psi(y, x) = \varphi^*(y, x)$  solving (2), where for each  $x$ ,  $u \mapsto \varphi(u, x)$  and  $y \mapsto \psi(y, x)$  are convex and Legendre conjugates:*

$$\varphi(u, x) = \sup_{y \in \mathcal{Y}} \{u^\top y - \psi(y, x)\}, \quad \psi(y, x) = \varphi^*(y, x) = \sup_{u \in \mathcal{U}} \{u^\top y - \varphi(u, x)\}. \quad (3)$$

(ii) *The conditional vector quantile is  $Q_{Y|X}(u, x) = \nabla_u \varphi(u, x)$  for  $F_U$ -a.e.  $u$ .*

(iii) *The conditional vector rank is  $Q_{Y|X}^{-1}(y, x) = \nabla_y \psi(y, x)$  for  $F_{Y|X}(\cdot, x)$ -a.e.  $y$ .*

(iv) *These maps are inverses: for each  $x$ ,  $\nabla_y \psi(\nabla_u \varphi(u, x), x) = u$ ,  $\nabla_u \varphi(\nabla_y \psi(y, x), x) = y$ , for  $F_U$ -a.e.  $u$  and  $F_{Y|X}(\cdot, x)$ -a.e.  $y$ .*

This theorem gives us necessary tools for the practical solution of OT problem (2).

We now introduce the proposed approach for learning continuous Neural VQR models. First, we reformulate the optimization problem as a function of a unique (convex) potential using the conditional  $c$ -transform. We then discuss how this problem can be solved in practice using Partially Input Convex Neural Networks (PICNNs; Amos et al., 2017) and how their training can be accelerated by amortized optimization.

**Neural parameterization and semi-dual formulation.** First, following Taghvaei & Jalali (2019); Makkouva et al. (2020); Amos (2023), we propose to reformulate the Monge-Kantorovich dual problem (2) as an optimization problem over a parametric family of potentials  $\varphi_\theta$  with parameters  $\theta$ . Since  $\varphi_\theta$  should be convex in its first argument, it is ensured that one can estimate a unique potential using the Fenchel-Legendre conjugacy in equation (3) (also called  $c$ -transform in the OT literature). We introduce for each  $x \in \mathcal{X}$  the conjugate of a pointwise potential  $\varphi_\theta(\cdot, x) : \mathcal{U} \rightarrow \mathcal{Y}$  as

$$J_{\varphi_\theta(\cdot, x)}(u, y) = u^\top y - \varphi_\theta(u, x), \quad (4)$$

$$\varphi_\theta^*(y, x) = J_{\varphi_\theta(\cdot, x)}(\check{u}_{\varphi_\theta(\cdot, x)}(y), y), \quad \check{u}_{\varphi_\theta(\cdot, x)}(y) = \arg \max_{u \in \mathcal{U}} J_{\varphi_\theta(\cdot, x)}(u, y). \quad (5)$$

With these notations, the problem (2) can be reformulated as the minimization of  $\mathcal{V}(\theta)$ , defined as

$$\mathcal{V}(\theta) := \mathbb{E}_{(U, X) \sim F_U \otimes F_X} [\varphi_\theta(U, X)] + \mathbb{E}_{(Y, X) \sim F_{Y|X}} [\varphi_\theta^*(Y, X)]. \quad (6)$$

Here,  $F_U \otimes F_X$  denotes the product measure of  $F_U$  and  $F_X$ , corresponding to independent sampling of  $U \sim F_U$  and  $X \sim F_X$ . The optimal parameter, can be found by taking gradient steps of the dual objective with respect to  $\theta$ . The derivative goes through the loss and the Fenchel-Legendre conjugate is obtained by applying Danskin's theorem (Danskin, 1967) and only requires the derivative of the potential

$$\nabla_\theta \mathcal{V}(\theta) = \mathbb{E}_{(U, X) \sim F_U \otimes F_X} [\nabla_\theta \varphi_\theta(U, X)] - \mathbb{E}_{(Y, X) \sim F_{Y|X}} [\nabla \varphi_\theta(u, X) \mid u = \check{u}_{\varphi_\theta(\cdot, x)}(Y)].$$

**Remark 1.** Above we discuss the optimization of the dual potential  $\varphi_\theta(\cdot, x)$  which is linked to  $F_U$ , with its conjugate  $\varphi_\theta^*(\cdot, x)$  is linked to  $F_{Y|X}(\cdot \mid X = x)$ . But in practice, due to the symmetry of (2), one can instead use  $\psi_\theta(\cdot, x)$ . In our experiments we investigate both strategies.

**Neural Quantile Regression with PICNNs (C-NQR).** The convexity of  $\varphi_\theta(\cdot, x)$  with respect to the first argument can be achieved (Bunne et al., 2022) by the usage of PICNNs (Amos et al., 2017)).

216 However, the remaining challenge in solving the optimization problem in (6) arises from the fact  
 217 that the conjugate  $\varphi_\theta^*(\cdot, x)$  must be computed for each  $x$  in the mini-batch. As a first strategy, we  
 218 propose to do this exactly with an L-BFGS solver (Liu & Nocedal, 1989). The parameters of the  
 219 PICNN potential  $\varphi_\theta$  can be optimized using stochastic gradient descent (SGD); see Algorithm 1 in  
 220 Appendix E.6 for implementation details. This approach is conceptually simple and uses existing  
 221 optimization tools. However, it can be computationally intensive due to the repeated optimization  
 222 required to compute the conjugates, especially for large mini-batches or high-dimensional data.

223 **Amortized Neural Quantile Regression (AC-NQR).** To reduce the computational cost of repeat-  
 224 edly solving the optimization problem (5) to compute the conjugates, we propose an amortized  
 225 optimization. The idea is to learn a predictor that approximates the solution of the conjugate prob-  
 226 lem, thus speeding up the inner optimization and training process. This strategy has been shown to  
 227 be effective in the non-conditional case by Amos (2023).

228 We extend this approach to the conditional case by introducing an amortization model  $\tilde{u}_\vartheta(y, x)$   
 229 parameterized by  $\vartheta$  that maps  $(y, x)$  to a point that should ideally be close to the true solution  
 230  $\tilde{u}_{\varphi_\theta(\cdot, x)}(y)$  in (5):

$$\tilde{u}_\vartheta(y, x) \simeq \tilde{u}_{\varphi_\theta(\cdot, x)}(y).$$

232 Note that different strategies have been proposed for the amortization model, but we will only focus  
 233 on the one based on PICNNs such as in (Makkuva et al., 2020; Korotin et al., 2019). The amorti-  
 234 zation model is trained jointly with the potential  $\varphi_\theta$  by optimizing a quadratic loss that makes  
 235  $\tilde{u}_\vartheta(y, x)$  to be close to  $\tilde{u}_{\varphi_\theta(\cdot, x)}(y)$ ; see Algorithm 2 in Appendix E.6 for implementation details.  
 236 This approach assumes that the amortization model evolves on a faster timescale than the potential  
 237  $\varphi_\theta$ , ensuring that its updates can track the slower dynamics of  $\varphi_\theta$  during training, following the  
 238 standard two-time-scale approximation (Konda & Tsitsiklis, 2004; Borkar, 2008).

239 **Entropic regularized Neural Quantile Regression (EC-NQR).** Note that the two approaches dis-  
 240 cussed above requires the solution of a convex optimization problem to compute the exact conju-  
 241 gates, which becomes computationally intensive in high-dimensions. An alternative approach is  
 242 to employ entropic regularization, enabling the use of stochastic gradient solvers (Genevay et al.,  
 243 2016), which scale well but introduce bias that may distort the geometry of quantile maps (Rosen-  
 244 berg et al., 2023). Using a neural network to estimate the dual potentials was considered by Seguy  
 245 et al. (2018) for the non-conditional case and we propose to extend it to the conditional case for  
 246 Neural VQR.

247 This is done by adding an entropic regularization term to the primal OT problem, which smooths  
 248 the problem and provides a closed-form solution for the conjugate (the argmax in (5) becomes  
 249 a softmax). This approach replaces the convex optimization required for conjugate optimization  
 250 by an expectation that can be approximated with sampling; see Algorithm 3 in Appendix E.6 for  
 251 implementation details. More details on this approach and related works can be found in Appendix C  
 252 and Appendix A respectively.

## 254 4 CONFORMAL PREDICTION WITH OT NEURAL MAPS

256 In this section, we demonstrate the use of our neural OT framework in constructing intrinsically  
 257 adaptive confidence sets with CP. The key idea is to exploit multivariate quantile and rank maps  
 258 learned by conditional neural OT as a building block for defining conformity scores and constructing  
 259 calibrated prediction regions. Let  $(Y, X) \sim F_{YX}$  and  $\alpha \in (0, 1)$  and denote by  $\hat{Q}_{Y|X}^{-1}$  a proxy for  
 260 the true associated vector rank function  $Q_{Y|X}^{-1}$  as in Theorem 1.

262 **Generalizing conformalized quantile regression.** In the univariate case, conformalized quantile  
 263 regression (CQR; Romano et al., 2019) replaces a nominal quantile with the empirical  $(1 - \alpha)$ -  
 264 quantile of residuals, ensuring distribution-free, finite-sample coverage. The same principle extends  
 265 to the plug-in pullback set in (1). Define conformity scores

$$S_i = \|\hat{Q}_{Y|X}^{-1}(Y_i, X_i)\|, \quad (Y_i, X_i) \in \mathcal{D}_{\text{cal}}.$$

266 Let  $S_{(1)} \leq \dots \leq S_{(n)}$  denote the order statistics, set  $k = \lceil (n+1)(1 - \alpha) \rceil$ , and  $\rho_{1-\alpha} = S_{(k)}$ . The  
 267 conformal set

$$\hat{\mathcal{C}}_\alpha^{\text{pb}}(x) = \{y: \hat{Q}_{Y|X}^{-1}(y, x) \in B(0, \rho_{1-\alpha})\}$$

270 then guarantees  $\mathbb{P}_{(Y,X) \sim F_{Y|X}}(Y \in \hat{\mathcal{C}}_\alpha^{\text{pb}}(X)) \geq 1 - \alpha$ . We now show that this construction of  
 271 confidence sets is optimal when the Jacobian of the inverse transport admits a radial structure.

272 **Theorem 3** (Volume–optimality of pullback balls under radiality). *Fix  $x \in \mathcal{X}$  and reference distribution  
 273  $F_U(u) = \phi(\|u\|)$  for a strictly decreasing  $\phi: [0, \infty) \rightarrow (0, \infty)$  on  $\mathcal{U}$ , under the assumptions  
 274 of Theorem 1, let  $Q_{Y|X}$  and  $Q_{Y|X}^{-1}$  be the vector quantile and multivariate rank functions. Assume  
 275 that there exists  $j_x$  such that for all  $y$  in the support of  $F_{Y|X}$ , it holds*

$$277 \det \left[ \nabla_y Q_{Y|X}^{-1}(y, x) \right] = j_x \left( \|Q_{Y|X}^{-1}(y, x)\| \right),$$

279 and the function  $r \mapsto \phi(r) j_x(r)$  is strictly decreasing. Let  $r_\alpha > 0$  be the unique radius satisfying  
 280  $\mu(B_{r_\alpha}) = 1 - \alpha$ , where  $\mu$  is the law corresponding to  $F_U$  and  $B_r = \{u: \|u\| \leq r\}$ . Define  
 281 the pullback ball  $\mathcal{C}_\alpha^{\text{pb}}(x) := \{y: \|Q_{Y|X}^{-1}(y, x)\| \leq r_\alpha\}$ . Then,  $\mathcal{C}_\alpha^{\text{pb}}(x)$  minimizes Lebesgue volume  
 282 among all sets with  $x$ -conditional coverage of at least  $1 - \alpha$ , i.e., for every measurable  $A \subset \mathcal{Y}_x$  with  
 283  $\mathbb{P}\{Y \in A \mid X = x\} \geq 1 - \alpha$ ,  $\text{Vol}(\mathcal{C}_\alpha^{\text{pb}}(x)) \leq \text{Vol}(A)$ .

284 Equivalently, Theorem 3 shows that  $\mathcal{C}_\alpha^{\text{pb}}(x)$  is the highest probability density (HPD) region for  
 285  $Y \mid X = x$  at level  $1 - \alpha$ . A noteworthy specialization, where the assumptions of Theorem 3 are  
 286 met, is the *elliptical* case (including Gaussian) with  $F_{Y|X}$  and  $F_U$  belonging to the same elliptical  
 287 family. We defer the proof and additional details to Appendix F.

289 **Re-ranked pullback sets.** This construction is effective only if the scores  $S_i$  capture isotropic  
 290 structure. Indeed,  $\hat{\mathcal{C}}_\alpha^{\text{pb}}(x)$  is the preimage of a centered Euclidean ball in  $\mathcal{U}$ , implicitly assuming that  
 291 the conditional distribution of  $U = \hat{Q}_{Y|X}^{-1}(Y, X)$  is radially symmetric. When  $\hat{Q}_{Y|X}^{-1}$  is misspecified,  
 292 however, the ranks may be anisotropic, and Euclidean radii become unreliable. We note that the  
 293 vector ranks  $\{U_i = \hat{Q}_{Y|X}^{-1}(Y_i, X_i)\}_{i=1}^n$  can themselves be interpreted as multivariate score functions  
 294 and as such be combined with the OT-CP approach of Thurin et al. (2025), which is designed to  
 295 conformalize multivariate score functions. In particular, let  $\mathbf{R}: \mathcal{U} \rightarrow \mathcal{U}$  be a reranking approach,  
 296 designed to correct deviations from reference distribution  $F_U$ . Then, the conformalization step may  
 297 be applied to the adjusted scores  $\|\mathbf{R}(U_i)\|$ , yielding a calibrated radius  $\rho_{1-\alpha}^{\text{uni}}$  and the prediction set  
 298

$$299 \hat{\mathcal{C}}_\alpha^{\text{rpb}}(x) = \{y: \mathbf{R}(\hat{Q}_{Y|X}^{-1}(y, x)) \in \hat{\mathcal{Q}}(1 - \alpha)\},$$

300 where  $\hat{\mathcal{Q}}(1 - \alpha) = \{u: \|\mathbf{R}(u)\| \leq \rho_{1-\alpha}^{\text{uni}}\}$ . See additional implementation details in Appendix E.7  
 301 *Remark 2.* For completeness, we also consider a complementary construction that leverages the  
 302 OT quantile and rank maps to estimate the conditional density via the change of variables formula.  
 303 Using the estimated density as a conformal score, this approach yields valid regions and can capture  
 304 disconnected geometry when  $F_{Y|X=x}$  is multimodal, e.g. Gaussian mixture. We provide additional  
 305 details and a brief discussion in Appendix F.

## 307 5 RELATED WORK

310 **Multivariate Quantiles.** Scalar quantile regression estimates conditional quantiles of  $Y \in \mathbb{R}$  given  
 311  $X \in \mathbb{R}^p$ , typically using linear-in-features models trained via the check loss (Koenker & Bassett,  
 312 1978; Koenker, 2005). Extending this framework to the multivariate setting is challenging due to the  
 313 absence of a natural total order. Early generalizations include spatial quantiles (Chaudhuri, 1996)  
 314 and depth-based quantiles (Hallin et al., 2021), though these lack a transport-map interpretation.  
 315 From a measure-transportation perspective, multivariate quantiles are defined as optimal transport  
 316 (OT) maps from a reference distribution, inducing center-outward ranks and quantile regions with  
 317 desirable geometric and statistical properties (Chernozhukov et al., 2017; Hallin et al., 2021; Hallin  
 318 & Konen, 2024; del Barrio et al., 2025). The conditional vector quantile function (CVQF) of Carlier  
 319 et al. (2016) models the quantile map as affine in  $X$  and estimates it via variational OT (Carlier  
 320 et al., 2017), with subsequent extensions to nonlinear embeddings (Rosenberg et al., 2023) and non-  
 321 parametric rank estimation (del Barrio et al., 2025). However, prior efforts to construct continuous  
 322 VQR models (Vedula et al., 2023b;a; Sun et al., 2022) have retained the affine-in- $X$  assumption,  
 323 thereby constraining the expressivity of the learned quantile maps. Moreover, these methods do not  
 324 provide a principled way to estimate continuous rank functions, instead producing discrete, point-  
 325 wise solutions. Finally, while scalable solvers based on entropic regularization have been developed,

324 to the best of our knowledge, no previous work has scaled VQR using neural optimal transport, as  
 325 proposed in this paper.

327 **Neural Optimal Transport.** High-dimensional OT is challenging due to the nonlinear dual formulation.  
 328 One approach employs entropic regularization, enabling Sinkhorn iterations and stochastic  
 329 gradient solvers (Cuturi, 2013; Genevay et al., 2016; Seguy et al., 2018; Carlier et al., 2022), which  
 330 scale well but introduce bias that may distort the geometry of quantile maps (Rosenberg et al.,  
 331 2023). A second approach parameterizes convex potentials with input-convex neural networks (IC-  
 332 NNs; Amos et al., 2017; Makkula et al., 2020; Amos, 2023), ensuring monotonicity and invertibility  
 333 of the learned map. Conditional potentials (and Monge maps) have been proposed in Bunne et al.  
 334 (2022) but are learned in a supervised way (from examples of conditioning and target distributions)  
 335 and never from a unique joint sampling using the framework of Carlier et al. (2017) as proposed in  
 336 our work.

337 **Multivariate Conformal Prediction.** Conformal prediction (CP) constructs distribution-free pre-  
 338 dictive sets with coverage guarantees. In the scalar case, conformalized quantile regression (CQR;  
 339 Shafer & Vovk, 2008; Romano et al., 2019; Angelopoulos et al., 2023) adjusts quantile estimates  
 340 to achieve valid intervals. For multivariate responses, naive coordinatewise CP yields conservative  
 341 rectangles; scalarized scores via norms or maxima produce balls or boxes, but remain restrictive.  
 342 Structured approaches include deep generative embeddings (Feldman et al., 2023) and copula cali-  
 343 brations (Messoudi et al., 2021). Dheur et al. (2025) propose conformity scores based on generative  
 344 models or aggregated  $p$ -values.

345 In contrast with previously developed methods based on generative modeling (Feldman et al., 2023;  
 346 Dheur et al., 2025). We propose an explicit generative model, that approximates a canonical quantile  
 347 function (Hallin et al., 2021). The fact that the transformation is cyclically monotone is crucial for  
 348 defining a statistically meaningful notion of multivariate rank (see Appendix G).

349 Very recently, the use of OT-based ranks and quantiles has been exploited in conformal prediction.  
 350 In two concurrent works, Thurin et al. (2025) define conformity scores from discrete OT ranks,  
 351 while Klein et al. (2025) leverage the same construction albeit with entropy regularized discrete OT.  
 352 By construction, these two approaches are not adaptive, i.e. the size of the conformal set does not  
 353 depend on  $X$ . Nonetheless, Thurin et al. (2025) propose an adaptive variant based on conditional  
 354 with  $k$  nearest neighbors. Our direct learning of neural VQR does not depend on conditional density  
 355 estimation and should perform better in high dimensionality settings.

## 357 6 NUMERICAL EXPERIMENTS

### 360 6.1 NEURAL OPTIMAL TRANSPORT

361 To evaluate the generative performance of our models, we conduct extensive experiments. Whenever  
 362 a ground-truth operator is required, we parametrize the datasets using a convex potential function,  
 363 see Appendix H.2 for details. EC-NQR, C-NQR $_U$ , C-NQR $_Y$ , AC-NQR $_U$ , AC-NQR $_Y$  are the meth-  
 364 ods described in Section 4. We measure the generative performance against FN-VQR (Rosenberg  
 365 et al., 2023), VQR (Carlier et al., 2017), CPF (Huang et al., 2021), (Vedula et al., 2023a) and (Sun  
 366 & Yu, 2024).

367 **Metrics.** We employ three categories of metrics: (i) Wasserstein-2 (W2) and Sliced Wasserstein-2  
 368 (S-W2) distances; (ii) Kernel Density Estimate  $\ell_1$  distance (KDE-L1) and Kernel Density Estimate  
 369 Kullback–Leibler divergence (KDE-KL); and (iii) Percentage of Unexplained Variance (L2-UV; Ko-  
 370 rotin et al., 2021). Metrics in (i) and (ii) quantify the fidelity of the learned distribution to the target  
 371 density, while (iii) assesses the extent to which the ground-truth quantile is recovered. Additional  
 372 implementation details are provided in Appendix H.2.

373 **Datasets.** We evaluate on three synthetic datasets originally introduced in the discrete setting of  
 374 quantile regression (Rosenberg et al., 2023): *Banana*, a parabola-shaped distribution whose curva-  
 375 ture varies with a latent random variable; *Star*, a three-pointed star whose orientation is governed by  
 376 a latent variable; and *Glasses*, a bimodal distribution with sinusoidally shifting modes. We denote  
 377 convex-potential counterparts as *Convex Banana*, *Convex Star*, and *Convex Glasses*.

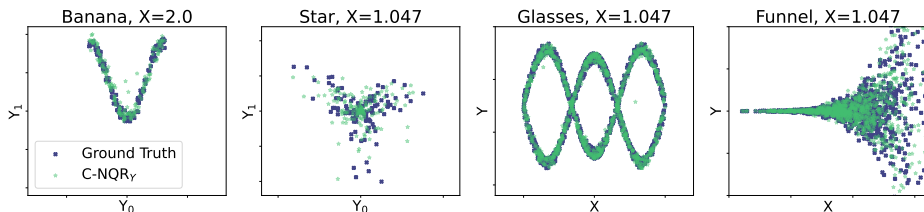


Figure 1: Example of points sampled from reference distribution of all the datasets we study and points sampled from approximation constructed by  $C\text{-}NQR_U$  method.

Dataset	EC-NQR	$C\text{-}NQR_U$	$C\text{-}NQR_Y$	$AC\text{-}NQR_U$	$AC\text{-}NQR_Y$	CPF	FN-VQR	VQR	Sun et al. (2022)	Vedula et al. (2023a)
Star	0.197	<b>0.184</b>	0.184	<b>0.182</b>	0.197	0.247	0.271	0.270	<b>0.274</b>	0.443
Glasses	<b>0.748</b>	0.785	0.812	<b>0.771</b>	0.810	1.687	2.017	1.964	<b>0.931</b>	1.170
Banana	0.111	0.072	0.073	0.073	<b>0.072</b>	<b>0.069</b>	0.398	0.389	<b>0.237</b>	0.401
Convex Star	0.200	<b>0.182</b>	0.184	<b>0.182</b>	0.191	0.191	0.262	0.261	<b>0.252</b>	0.448
Convex Glasses	<b>0.650</b>	<b>0.656</b>	0.668	0.657	0.689	0.760	1.954	1.961	<b>0.793</b>	0.953
Convex Banana	0.103	0.101	0.071	<b>0.070</b>	0.070	<b>0.069</b>	0.397	0.392	<b>0.211</b>	0.425
Training time	10.99 sec.	15.08 sec.	15.09 sec.	8.89 sec.	12.63 sec.	-	-	-	-	-
Inference time	1.71 sec.	1.21 sec.	1.76 sec.	1.12 sec.	1.34 sec.	-	-	-	-	-

Table 1: S-W2 between ground truth and empirical distributions. We provide training time per epoch that is averaged over all the datasets and average inference time for computing c-transform inverse of 8192 elements. **We mark the best result with bold text and the second best result with underscore.**

Function	Dataset	EC-NQR	$C\text{-}NQR_U$	$C\text{-}NQR_Y$	$AC\text{-}NQR_U$	$AC\text{-}NQR_Y$	CPF
$Q_{Y X}^{-1}$	Convex Star	1.331	<b>0.211</b>	0.286	<b>0.264</b>	0.425	0.447
	Convex Glasses	0.348	0.332	<b>0.068</b>	0.203	<b>0.109</b>	2.268
	Convex Banana	3.942	3.784	0.212	<b>0.106</b>	<b>0.206</b>	9.479
$Q_{U X}$	Convex Star	2.746	0.360	<b>0.351</b>	0.393	0.525	<b>0.267</b>
	Convex Glasses	<b>0.678</b>	<b>0.535</b>	0.732	0.985	1.096	1.726
	Convex Banana	9.400	7.665	0.660	<b>0.545</b>	<b>0.569</b>	16.537

Table 2: L2-UV of the true quantile function measured on generative processes parameterized by convex potential networks. **We mark the best result with bold text and the second best result with underscore.**

Lastly, we consider Neal’s Funnel (Neal, 2003) Figure 1. We extend this benchmark to higher dimensions by sampling  $n$  independent samples from the distributions.

**Results.** We denote by  $C\text{-}NQR_U$  and  $AC\text{-}NQR_U$  the models estimating  $\varphi(u, x)$ , and by  $C\text{-}NQR_Y$  and  $AC\text{-}NQR_Y$  the models estimating  $\psi(y, x)$ ; see equation (2). The experiments evaluate the generative capability of the proposed neural quantile regression framework. Numerical results demonstrate that the learned transport maps are accurate, and scale with the dimensions.

To evaluate scalability, Figure 2 reports the S-W2 metric on Neal’s Funnel as the target dimension increases from 2 to 16. We observe that methods leveraging explicit c-transform computation ( $NQR_U$ ,  $NQR_Y$ ,  $AC\text{-}NQR_U$ ,  $AC\text{-}NQR_Y$ ) scale robustly with dimensionality and maintain high generative accuracy, while entropically relaxed variants (EC-NQR) fail to scale effectively. Furthermore, the proposed framework consistently achieves superior S-W2 metric compared to prior approaches (Rosenberg et al., 2023; Carlier et al., 2016), demonstrating its performance in high-dimensional quantile estimation.

Finally, we evaluate the ability of our method to recover the underlying quantile mapping. We report the L2-UV metric in Table 2 evaluated on Convex Banana, Convex Star, and Convex Glasses. The results in Table 2 show that the proposed models achieve high precision in reconstructing the true quantile operator.

The experiments confirm the overall performance of the proposed quantile construction, making it a suitable tool for subsequent conformal prediction procedures.

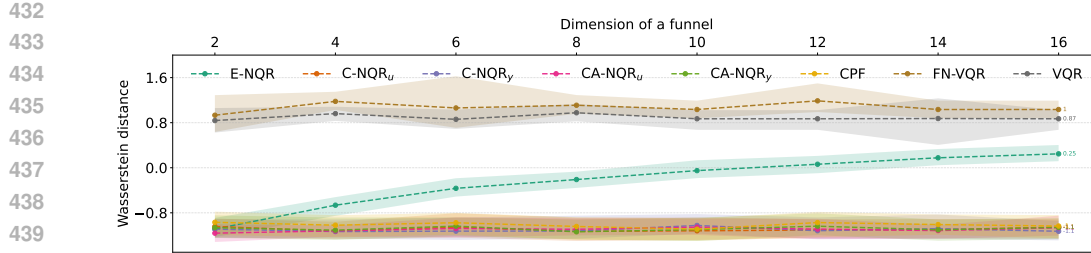


Figure 2: Log values of  $S\text{-W2}$  on Neal’s funnel distribution. We scale the dimension of a funnel from 2 to 16.

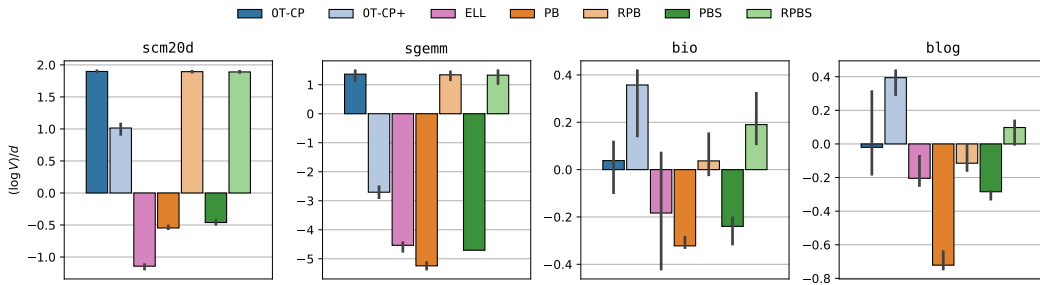


Figure 3: Log-volume of the prediction sets, normalized by  $d_y$ , of the resulting prediction sets for different methods. Results averaged over 10 independent data splits. Nominal miscoverage level  $\alpha = 0.1$

## 6.2 CONFORMAL PREDICTION EXPERIMENTS

We further evaluate conformal prediction by constructing prediction sets on real-world datasets using the methods described in Section 4. Extended results are presented in Appendix H.

**Methods.** We use AC-NQR<sub>U</sub> as the base model to implement our two conformal methods: PB( $\hat{\mathcal{C}}^{\text{pb}}$ ) and RPB( $\hat{\mathcal{C}}^{\text{rpb}}$ ). In addition to fitting our vector quantile regression model directly on  $y$ , we also fit both methods on signed residuals  $s = y - \hat{f}(x)$ , where  $\hat{f}$  is a Random Forest regressor fit on 25% of the training data (PBS and RPBS in the plots). We consider OT-CP and OT-CP+ (Thurin et al., 2025), as well as the local Ellipsoid method (Messoudi et al., 2022) for comparison.

**Metrics.** We evaluate performance using three metrics: (i) marginal coverage, (ii) worst-slab coverage (Cauchois et al., 2021), and (iii) average prediction set volume.

**Datasets.** We evaluate on standard multi-target regression benchmarks used in previous work on uncertainty estimation (Plassier et al., 2025; Dheur et al., 2025): scm20d, sgemm, blog, and bio. For the single-target datasets blog and bio, we follow Feldman et al. (2023) and add one of the features as a second output. The resulting response dimensions are 16, 4, 2 and 2, respectively. We use preprocessing procedure of (Grinsztajn et al., 2022).

**Discussion.** PB and PBS provide competitive conditional coverage and smallest volume at the same time on three out of four datasets. The re-ranking step of RPB and RPBS allows to achieve a slightly sharper conditional coverage, but the increase in prediction sets volume make it a questionable trade-off. Overall, it shows that for our quantile regression models the split conformal calibration is enough. Our methods provide a scalable training enable building competitive conformal predictors.

## 7 CONCLUSION

We introduced a framework for multivariate conformal prediction based on convex potentials and optimal transport. Our approach leverages neural quantile regression with input convex neural network parameterization to construct valid and efficient prediction sets. Through experiments on synthetic benchmarks and real-world multi-target regression datasets, we demonstrated strong performance

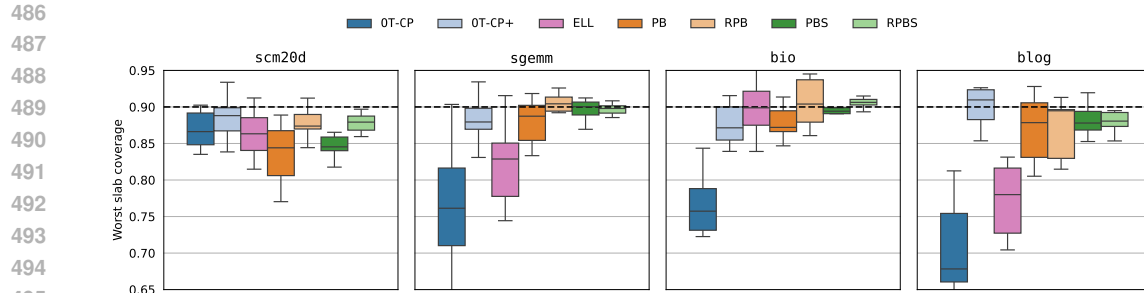


Figure 4: Worst-slab coverage for different methods. Results averaged over 10 independent data splits. Nominal miscoverage level  $\alpha = 0.1$

in terms of coverage and set size, while maintaining scalability in higher dimensions. Comparisons with existing baselines further highlight the robustness and flexibility of our method. Future work includes extending the framework to broader classes of generative models and exploring tighter efficiency guarantees in high-dimensional regimes.

503  
504  
505  
506  
507  
508  
509  
510  
511  
512  
513  
514  
515  
516  
517  
518  
519  
520  
521  
522  
523  
524  
525  
526  
527  
528  
529  
530  
531  
532  
533  
534  
535  
536  
537  
538  
539

540 **USAGE OF LARGE LANGUAGE MODELS (LLMs)**  
541542 LLMs were used as a general-purpose assistive tool during the preparation of this paper. Their us-  
543 age fell into two categories: (i) for writing assistance, they helped improve clarity and readability  
544 of certain passages through language refinement and (ii) for coding assistance, where they provided  
545 support with code completion and debugging. LLMs were not used for research ideation, experimen-  
546 tal design, theoretical development, or analysis of results. All substantive contributions, including  
547 the conception of ideas, methodology, and experiments, were made by the authors.  
548549 **REPRODUCIBILITY STATEMENT**  
550551 We provide the full code to reproduce our experiments as supplementary material and will release it  
552 publicly upon acceptance. All experiments were conducted on publicly available datasets or datasets  
553 we created ourselves, which will be released alongside the code. We ran experiments with multiple  
554 seeds, if applicable, and report summary statistics.  
555556 **REFERENCES**  
557

558 Brandon Amos. On amortizing convex conjugates for optimal transport. In *The Eleventh Interna-*  
559 *tional Conference on Learning Representations*, 2023.

560 Brandon Amos, Lei Xu, and J Zico Kolter. Input convex neural networks. In *International Confer-*  
561 *ence on Machine Learning*, pp. 146–155. PMLR, 2017.

563 Anastasios N Angelopoulos, Stephen Bates, et al. Conformal prediction: A gentle introduction.  
564 *Foundations and Trends® in Machine Learning*, 16(4):494–591, 2023.

565 Vivek S Borkar. *Stochastic approximation: a dynamical systems viewpoint*. Springer, 2008.

567 Axel Brando, Barcelona Supercomputing Center, José Rodríguez-Serrano, Jordi Vitrià, et al. Deep  
568 non-crossing quantiles through the partial derivative. In *International Conference on Artificial*  
569 *Intelligence and Statistics*, pp. 7902–7914. PMLR, 2022.

570 Sacha Braun, Liviu Aolaritei, Michael I. Jordan, and Francis Bach. Minimum volume conformal  
571 sets for multivariate regression. *arXiv:2503.19068*, 2025.

573 Yann Brenier. Polar factorization and monotone rearrangement of vector-valued functions. *Commu-*  
574 *nications on Pure and Applied Mathematics*, 44(4):375–417, 1991.

575 Charlotte Bunne, Andreas Krause, and Marco Cuturi. Supervised training of conditional monge  
576 maps. In *Advances in Neural Information Processing Systems*, volume 35, pp. 6859–6872, 2022.

578 Guillaume Carlier, Victor Chernozhukov, and Alfred Galichon. Vector quantile regression: An  
579 optimal transport approach. *The Annals of Statistics*, 44(3):1165 – 1192, 2016.

580 Guillaume Carlier, Victor Chernozhukov, and Alfred Galichon. Vector quantile regression beyond  
581 the specified case. *Journal of Multivariate Analysis*, 161:96–102, 2017.

583 Guillaume Carlier, Victor Chernozhukov, Gwendoline De Bie, and Alfred Galichon. Vector quantile  
584 regression and optimal transport, from theory to numerics. *Empirical Economics*, 62(1):35–62,  
585 2022.

586 Maxime Cauchois, Suyash Gupta, and John C Duchi. Knowing what you know: valid and validated  
587 confidence sets in multiclass and multilabel prediction. *Journal of Machine Learning Research*,  
588 22(81):1–42, 2021.

589 Probal Chaudhuri. On a geometric notion of quantiles for multivariate data. *Journal of the American*  
590 *Statistical Association*, 91(434):862–872, 1996. doi: 10.1080/01621459.1996.10476975.

591 Victor Chernozhukov, Alfred Galichon, Marc Hallin, and Marc Henry. Monge–kantorovich depth,  
592 quantiles, ranks and signs. *The Annals of Statistics*, 45(1):223–256, 2017. doi: 10.1214/  
593 16-AOS1450.

594 Marco Cuturi. Sinkhorn distances: Lightspeed computation of optimal transport. In *Advances in*  
 595 *Neural Information Processing Systems*, volume 26, 2013.  
 596

597 Nhan Dam, Quan Hoang, Trung Le, Tu Dinh Nguyen, Hung Bui, and Dinh Phung. Three-player  
 598 wasserstein gan via amortised duality. In *International Joint Conference on Artificial Intelligence*  
 599 2019, pp. 2202–2208. Association for the Advancement of Artificial Intelligence (AAAI), 2019.

600 John M. Danskin. *The Theory of Max-Min and Its Application to Weapons Allocation Problems*,  
 601 volume 5 of *Econometrics and Operations Research*. Springer-Verlag, Berlin, Heidelberg, 1967.  
 602

603 Eustasio del Barrio, Alberto González Sanz, and Marc Hallin. Nonparametric multiple-output  
 604 center-outward quantile regression. *Journal of the American Statistical Association*, 120(550):  
 605 818–832, 2025.

606 Victor Dheur, Matteo Fontana, Yorick Estievenart, Naomi Desobry, and Souhaib Ben Taieb. A  
 607 unified comparative study with generalized conformity scores for multi-output conformal regres-  
 608 sion. In *Proceedings of the 42nd International Conference on Machine Learning*, Proceedings of  
 609 Machine Learning Research. PMLR, 2025.

610 Nathaniel Diamant, Ehsan Hajiramezanali, Tommaso Biancalani, and Gabriele Scalia. Conformal-  
 611 ized deep splines for optimal and efficient prediction sets. In *International Conference on Artifi-  
 612 cial Intelligence and Statistics*, pp. 1657–1665. PMLR, 2024.

613 Jacopo Diquigiovanni, Matteo Fontana, and Simone Vantini. The importance of being a  
 614 band: Finite-sample exact distribution-free prediction sets for functional data. *arXiv preprint*  
 615 *arXiv:2102.06746*, 2021.

616 Zhenhan Fang, Aixin Tan, and Jian Huang. Contra: Conformal prediction region via normalizing  
 617 flow transformation. In *The Thirteenth International Conference on Learning Representations*,  
 618 2025.

619 Shai Feldman, Stephen Bates, and Yaniv Romano. Calibrated multiple-output quantile regression  
 620 with representation learning. *Journal of Machine Learning Research*, 24(24):1–48, 2023.

621 Rémi Flamary, Nicolas Courty, Alexandre Gramfort, Mokhtar Z. Alaya, Aurélie Boisbunon, Stanis-  
 622 las Chambon, Laetitia Chapel, Adrien Corenflos, Kilian Fatras, Nemo Fournier, Léo Gautheron,  
 623 Nathalie T.H. Gayraud, Hicham Janati, Alain Rakotomamonjy, Ievgen Redko, Antoine Rolet,  
 624 Antony Schutz, Vivien Seguy, Danica J. Sutherland, Romain Tavenard, Alexander Tong, and  
 625 Titouan Vayer. Pot: Python optimal transport. *Journal of Machine Learning Research*, 22(78):  
 626 1–8, 2021. URL <http://jmlr.org/papers/v22/20-451.html>.

627 Alfred Galichon. *Optimal Transport Methods in Economics*. Princeton University Press, Princeton  
 628 and Oxford, 2018.

629 Aude Genevay, Marco Cuturi, Gabriel Peyré, and Francis Bach. Stochastic optimization for large-  
 630 scale optimal transport. In *Advances in Neural Information Processing Systems*, volume 29, 2016.

631 Promit Ghosal and Bodhisattva Sen. Multivariate ranks and quantiles using optimal transport: Con-  
 632 sistency, rates and nonparametric testing. *The Annals of Statistics*, 50(2):1012–1037, 2022.

633 Léo Grinsztajn, Edouard Oyallon, and Gaël Varoquaux. Why do tree-based models still outperform  
 634 deep learning on typical tabular data? In *Advances in Neural Information Processing Systems*,  
 635 volume 35, pp. 507–520, 2022.

636 Marc Hallin and Dimitri Konen. Multivariate quantiles: Geometric and measure-transportation-  
 637 based contours. In *Applications of Optimal Transport to Economics and Related Topics*, pp.  
 638 61–78. Springer, 2024.

639 Marc Hallin and Miroslav Šiman. Multiple-output quantile regression. In Roger Koenker, Victor  
 640 Chernozhukov, Xin He, and Limin Peng (eds.), *Handbook of Quantile Regression*, pp. 185–207.  
 641 Chapman & Hall/CRC, 2017.

648 Marc Hallin, Eustasio Del Barrio, Juan Cuesta-Albertos, and Carlos Matrán. Distribution and quan-  
 649 tile functions, ranks and signs in dimension d: A measure transportation approach. *The Annals of*  
 650 *Statistics*, 49(2):1139–1165, 2021.

651 Chin-Wei Huang, Ricky TQ Chen, Christos Tsirigotis, and Aaron Courville. Convex potential flows:  
 652 Universal probability distributions with optimal transport and convex optimization. In *Inter-  
 653 national Conference on Learning Representations*, 2021.

654 Rafael Izbicki, Gilson T Shimizu, and Rafael B Stern. Flexible distribution-free conditional predic-  
 655 tive bands using density estimators. *arXiv preprint arXiv:1910.05575*, 2019.

656 Rafael Izbicki, Gilson Shimizu, and Rafael B Stern. Cd-split and hpd-split: Efficient conformal  
 657 regions in high dimensions. *Journal of Machine Learning Research*, 23(87):1–32, 2022.

658 Chancellor Johnstone and Bruce Cox. Conformal uncertainty sets for robust optimization. In *Con-  
 659 formal and Probabilistic Prediction and Applications (COPA)*, pp. 72–90, 2021.

660 Kelvin Kan, François-Xavier Aubet, Tim Januschowski, Youngsuk Park, Konstantinos Benidis, Lars  
 661 Ruthotto, and Jan Gasthaus. Multivariate quantile function forecaster. In *International Conference  
 662 on Artificial Intelligence and Statistics*, pp. 10603–10621. PMLR, 2022.

663 Durk P Kingma and Prafulla Dhariwal. Glow: Generative flow with invertible 1x1 convolutions. In  
 664 *Advances in Neural Information Processing Systems*, volume 31, 2018.

665 Michal Klein, Louis Bethune, Eugene Ndiaye, and Marco Cuturi. Multivariate conformal prediction  
 666 using optimal transport. *arXiv preprint arXiv:2502.03609*, 2025.

667 Martin Knott and Cyril S Smith. On the optimal mapping of distributions. *Journal of Optimization  
 668 Theory and Applications*, 43(1):39–49, 1984.

669 Roger Koenker. *Quantile Regression*. Econometric Society Monographs. Cambridge University  
 670 Press, 2005. doi: 10.1017/CBO9780511754098.

671 Roger Koenker and Gilbert Bassett. Regression quantiles. *Econometrica*, 46(1):33–50, 1978. doi:  
 672 10.2307/1913643.

673 Vijay R Konda and John N Tsitsiklis. Convergence rate of linear two-time-scale stochastic approxi-  
 674 mation. *The Annals of Applied Probability*, 14(2):796–819, 2004.

675 Alexander Korotin, Vage Egiazarian, Arip Asadulaev, Alexander Safin, and Evgeny Burnaev.  
 676 Wasserstein-2 generative networks. In *International Conference on Learning Representations*,  
 677 2019.

678 Alexander Korotin, Lingxiao Li, Aude Genevay, Justin M Solomon, Alexander Filippov, and Evgeny  
 679 Burnaev. Do neural optimal transport solvers work? a continuous wasserstein-2 benchmark. In  
 680 *Advances in Neural Information Processing Systems*, volume 34, pp. 14593–14605, 2021.

681 Dong C Liu and Jorge Nocedal. On the limited memory bfgs method for large scale optimization.  
 682 *Mathematical Programming*, 45(1):503–528, 1989.

683 Ashok Makkavu, Amirhossein Taghvaei, Sewoong Oh, and Jason Lee. Optimal transport mapping  
 684 via input convex neural networks. In *International Conference on Machine Learning*, pp. 6672–  
 685 6681. PMLR, 2020.

686 Soundouss Messoudi, Sébastien Destercke, and Sylvain Rousseau. Copula-based conformal predic-  
 687 tion for multi-target regression. *Pattern Recognition*, 120:108101, 2021.

688 Soundouss Messoudi, Sébastien Destercke, and Sylvain Rousseau. Ellipsoidal conformal inference  
 689 for multi-target regression. In *Conformal and Probabilistic Prediction and Applications (COPA)*,  
 690 pp. 294–306, 2022.

691 Radford M Neal. Slice sampling. *The Annals of Statistics*, 31(3):705–767, 2003.

692 Gabriel Peyré, Marco Cuturi, et al. Computational optimal transport: With applications to data  
 693 science. *Foundations and Trends® in Machine Learning*, 11(5-6):355–607, 2019.

702 Vincent Plassier, Alexander Fishkov, Victor Dheur, Mohsen Guizani, Souhaib Ben Taieb, Maxim  
 703 Panov, and Eric Moulines. Rectifying conformity scores for better conditional coverage. In  
 704 *Forty-second International Conference on Machine Learning*, 2025.

705

706 Ralph Tyrrell Rockafellar. *Convex Analysis*, volume 28 of *Princeton Mathematical Series*. Princeton  
 707 University Press, Princeton, NJ, reprint edition edition, 2015.

708

709 Yaniv Romano, Evan Patterson, and Emmanuel Candes. Conformalized quantile regression. In  
 710 *Advances in Neural Information Processing Systems*, volume 32, 2019.

711

712 Aviv A Rosenberg, Sanketh Vedula, Yaniv Romano, and Alexander Bronstein. Fast nonlinear vec-  
 713 tor quantile regression. In *The Eleventh International Conference on Learning Representations*,  
 2023.

714

715 Vivien Seguy, Bharath Bhushan Damodaran, Remi Flamary, Nicolas Courty, Antoine Rolet, and  
 716 Mathieu Blondel. Large scale optimal transport and mapping estimation. In *International Con-  
 717 ference on Learning Representations*, 2018.

718

719 Glenn Shafer and Vladimir Vovk. A tutorial on conformal prediction. *Journal of Machine Learning  
 Research*, 9(3), 2008.

720

721 Jesse Sun, Dihong Jiang, and Yaoliang Yu. Conditional generative quantile networks via optimal  
 722 transport. In *ICLR Workshop on Deep Generative Models for Highly Structured Data*, 2022.

723

724 Sophia Huiwen Sun and Rose Yu. Copula conformal prediction for multi-step time series prediction.  
 In *The Twelfth International Conference on Learning Representations*, 2024.

725

726 Amirhossein Taghvaei and Amin Jalali. 2-wasserstein approximation via restricted convex potentials  
 727 with application to improved training for gans. *arXiv preprint arXiv:1902.07197*, 2019.

728

729 Gauthier Thurin, Kimia Nadjahi, and Claire Boyer. Optimal transport-based conformal prediction.  
 In *Forty-second International Conference on Machine Learning*, 2025.

730

731 Sanketh Vedula, Irene Tallini, Aviv A Rosenberg, Marco Pegoraro, Emanuele Rodolà, Yaniv Ro-  
 732 mano, and Alexander Bronstein. Continuous vector quantile regression. In *ICML Workshop on  
 733 New Frontiers in Learning, Control, and Dynamical Systems*, 2023a.

734

735 Sanketh Vedula, Irene Tallini, Aviv A. Rosenberg, Marco Pegoraro, Emanuele Rodolà, Yaniv Ro-  
 736 mano, and Alexander M. Bronstein. Continuous vector quantile regression. In *ICML 2023 Work-  
 737 shop on New Frontiers in Learning, Control, and Dynamical Systems*, 2023b.

738

739 Zhendong Wang, Ruijiang Gao, Mingzhang Yin, Mingyuan Zhou, and David M. Blei. Probabilistic  
 740 conformal prediction using conditional random samples. In *Proceedings of the 26th International  
 741 Conference on Artificial Intelligence and Statistics (AISTATS)*, pp. 8814–8836, 2023.

742

743 Ruiyao Zhang, Ping Zhou, and Tianyou Chai. Improved copula-based conformal prediction for  
 744 uncertainty quantification of multi-output regression. *Journal of Process Control*, 129:103036,  
 745 2023.

746

747 Yanfei Zhou, Lars Lindemann, and Matteo Sesia. Conformalized adaptive forecasting of heteroge-  
 748 neous trajectories. *arXiv preprint arXiv:2402.09623*, 2024.

749

750

751

752

753

754

755

756 A EXTENDED STATE OF THE ART  
757

758 **From scalar to vector quantiles.** Classical quantile regression (QR) estimates conditional quantiles of a scalar response  $Y \in \mathbb{R}$  given features  $X \in \mathbb{R}^p$ , providing a flexible alternative to least  
759 squares for modeling heterogeneous effects (Koenker & Bassett, 1978; Koenker, 2005). For a  
760 quantile level  $u \in (0, 1)$  and feature map  $\varphi(x)$ , a standard linear QR model assumes  $Q_{Y|X}(u |$   
761  $x) = \beta(u)^\top \varphi(x)$ , with  $\beta(u)$  obtained by minimizing the check-loss. While univariate QR theory  
762 is well-developed, extending these notions to a multivariate response  $Y \in \mathbb{R}^d$  is challenging due  
763 to the lack of a natural total order on  $\mathbb{R}^d$ . Many generalizations have been proposed, including  
764 *directional* or *projection* quantiles (reducing to scalar quantiles along particular directions) and *ge-  
765 ometric* or *spatial* quantiles (e.g. Chaudhuri, 1996), as well as definitions based on statistical depth  
766 (e.g. Tukey’s halfspace depth) that yield central regions viewed as multivariate “quantiles.” How-  
767 ever, these early notions only partially extend scalar quantile properties and generally do not yield  
768 a unique quantile *mapping* for  $Y$ . A recent breakthrough comes from the *measure transportation*  
769 perspective, which defines multivariate quantiles as the optimal transport map pushing a reference  
770 distribution (usually the spherical uniform, or uniform on the unit hypercube) onto the distribution  
771 of  $Y$ . This approach rooted in Brenier’s theorem on monotone optimal transport maps (Brenier,  
772 1991) yields well-behaved center-outward distribution and quantile functions that assign each point  
773 in  $\mathbb{R}^d$  a multivariate rank and sign with distribution-free properties. The resulting quantile regions  
774 are nested, have correct probability contents, and enjoy equivariance properties generalizing the one-  
775 dimensional case. These concepts, introduced by Chernozhukov et al. (2017) and further developed  
776 by Hallin et al. (2021), provide a rigorous multivariate analog of the quantile function; see (Hallin  
777 & Šiman, 2017) for a survey of earlier definitions. Recent work continues to refine this frame-  
778 work: Hallin & Konen (2024) compare geometric vs. transport-based contours, and nonparametric  
779 multiple-output quantile regression methods based on center-outward ranks have been proposed (del  
780 Barrio et al., 2025).

781 **Vector quantile regression (VQR).** Building on optimal transport ideas, Carlier et al. (2016) in-  
782 troduced the *conditional vector quantile function* (CVQF)  $Q_{Y|X}(u, x)$  for  $Y \in \mathbb{R}^d$ . This is defined  
783 as a (a.e.) *monotone* map in  $u$  — specifically, the gradient of a convex function in the  $u$  argu-  
784 ment — such that for each fixed  $x$ ,  $Q_{Y|X}(\cdot, x)$  pushes the uniform distribution on  $[0, 1]^d$  forward  
785 to the conditional distribution  $Y | X = x$ . In analogy to the scalar case, one can represent  $Y$  as  
786  $Y = Q_{Y|X}(U, X)$  with  $U \sim \text{Unif}([0, 1]^d)$  independent of  $X$ . This generalizes the scalar quan-  
787 tile relationship  $Y = Q_{Y|X}(U, X)$  for  $U \sim \text{Unif}(0, 1)$ , providing a powerful characterization of  
788 the conditional law of  $Y$  by a deterministic map on the unit hypercube. In practice, VQR imposes  
789 a parametric form on the CVQF; for example, the original proposal assumes an affine structure  
790  $Q_{Y|X}(u, x) = \alpha(u) + B(u)^\top x$  (with  $\alpha(u) \in \mathbb{R}^d$  and  $B(u) \in \mathbb{R}^{d \times p}$ ) and estimates these functions  
791 by solving a large-scale optimal transport problem under empirical data constraints. The solution  
792 can be found via a convex dual formulation analogous to Koenker’s linear program, ensuring the  
793 fitted  $Q_{Y|X}$  is monotone in  $u$  (i.e. cyclically monotonic) (Carlier et al., 2016; 2017). This yielded  
794 the first notion of “quantile regression for vectors,” including strong theoretical guarantees on con-  
795 sistency and uniqueness under appropriate conditions. Since then, a number of extensions have been  
796 proposed: Rosenberg et al. (2023) introduce a fast nonlinear VQR model (e.g. using kernel or neural  
797 network features) while preserving monotonicity, Vedula et al. (2023b) develop a continuous VQR  
798 formulation that treats  $u$  in a continuum (rather than on a finite grid of quantile levels), and fully  
799 nonparametric approaches based on center-outward quantile functions have appeared (del Barrio  
800 et al., 2025). Each of these methods seeks to balance flexibility and computational tractability while  
801 maintaining the defining property that  $u \mapsto Q_{Y|X}(u, x)$  is a gradient map (hence invertible and  
802 order-preserving in the multivariate sense).

803 **Computation.** Implementing VQR at scale poses significant challenges. The initial algorithms  
804 of Carlier et al. (2016) and Carlier et al. (2017) relied on discretizing the unit hypercube  $[0, 1]^d$  (for  
805 a set of representative  $u$  values) and solving a large linear program, which becomes computationally  
806 expensive as  $d$  or the number of quantile levels grows. Two recent strategies have substantially  
807 improved the scalability of VQR. First, Carlier et al. (2022) propose an *entropic regularization*  
808 of the OT problem, which smooths the objective and leads to a differentiable dual formulation.  
809 By applying Sinkhorn-type iterations or gradient-based optimization on the regularized dual, one  
810 can efficiently approximate the CVQF without solving a huge LP, even for continuous  $u$  spaces.

810 This regularized VQR approach yields an accuracy–computational cost trade-off controlled by the  
 811 entropy penalty, and it has demonstrated orders-of-magnitude speedups on moderate-dimensional  
 812 problems.

813 The second approach uses deep learning to represent the convex potential of the CVQF: Makkula  
 814 et al. (2020) propose to parameterize  $Q_{Y|X}(u, x)$  as  $\nabla_u \psi(u, x)$  where  $\psi$  is an input-convex neural  
 815 network in  $u$ . By training  $\psi$  on data (using a suitable loss derived from the OT characterization),  
 816 one obtains a VQR model that can handle high-dimensional  $X$  and  $Y$  and large sample sizes. This  
 817 method, part of a broader trend of using neural networks for OT map estimation, sidesteps explicit  
 818 discretization by leveraging automatic differentiation to enforce convexity in  $u$ . Both the entropic-  
 819 OT and ICNN-based approaches have made it feasible to learn multivariate quantile functions on  
 820 modern datasets, a task once thought impractical (Huang et al., 2021; Kan et al., 2022). For additional  
 821 background on scalable optimal transport techniques that underlie these advances, see (Peyré  
 822 et al., 2019).

823  
 824 **Conformal prediction.** Conformal prediction (CP) provides distribution-free predictive uncer-  
 825 tainty sets with finite-sample coverage guarantees. In the scalar  $Y$  case, it is common to combine  
 826 quantile regression with conformal calibration. For example, conformalized quantile regression  
 827 (CQR) uses holdout data to adjust the initially estimated interval  $[\hat{Q}_{Y|X}(\alpha/2 | x), \hat{Q}_{Y|X}(1 - \alpha/2 |$   
 828  $x)]$  so that it achieves the target coverage  $1 - \alpha$  marginally. CQR and related methods yield prediction  
 829 intervals that are adaptive (varying with  $x$ ) while retaining rigorous coverage guarantees (Romano  
 830 et al., 2019; Angelopoulos et al., 2023). However, extending CP to multivariate outputs has proven  
 831 more complex. Naively applying conformal methods to each component of  $Y = (Y_1, \dots, Y_d)$  and taking a  
 832 Cartesian product of marginal intervals yields a rectangular prediction region that is valid but often overly  
 833 conservative (covering significantly more than  $1 - \alpha$  of the probability). More refined strategies have been  
 834 proposed to account for dependence between coordinates. One line of work defines a scalar nonconformity score from the multi-output residual, for instance using a norm  
 835  $|Y_{\text{pred}} - Y_{\text{true}}|$  or the maximum deviation across coordinates; this yields prediction balls or boxes  
 836 aligned to the chosen norm. While simple, such choices typically lead to symmetric or axis-aligned  
 837 regions that may be suboptimal in shape and volume. For example, the PCP method of Wang et al.  
 838 (2023) leverages an implicit generative model to draw random samples from  $Y | X = x$  and constructs  
 839 the prediction set as a union of Euclidean balls (of a fixed radius) centered at those samples. This  
 840 approach guarantees marginal coverage and can improve sharpness over naive intervals, but using a  
 841 global radius for all  $x$  can lead to over-coverage in low-variability regions and under-coverage in  
 842 high-variability regions. Alternatively, some works shape the prediction set as an ellipsoid by  
 843 incorporating covariance structure: e.g. using a single global covariance estimate (Johnstone &  
 844 Cox, 2021) or a local covariance around  $x$  (Messoudi et al., 2022) to define a Mahalanobis-distance  
 845 conformity score. Such ellipsoidal regions capture linear correlations in  $Y$  and are typically smaller  
 846 than axis-aligned boxes, but they still assume an (approximately) elliptical and unimodal error  
 847 distribution, which may be inappropriate for complex multimodal targets.

848 Another class of methods seeks to learn a joint representation or dependency model for  $Y$  before  
 849 applying conformal. For example, Feldman et al. (2023) train a deep generative model to embed  $Y$   
 850 into a lower-dimensional (ideally unimodal) latent space and perform conformal quantile regression  
 851 in that space, producing flexible regions when mapped back to  $\mathbb{R}^d$ . Similarly, Messoudi et al. (2021)  
 852 and subsequent works leverage copula transformations: they calibrate marginal predictive intervals  
 853 at miscoverage levels chosen to optimize the volume of the resulting joint region, effectively shaping  
 854 the prediction set according to the dependence structure of  $Y$ . In particular, Zhang et al. (2023)  
 855 extend copula-based conformal prediction by allowing different significance levels for each output  
 856 dimension and directly optimizing the hyperrectangle volume under the coverage constraint. Sun  
 857 & Yu (2024) provide a theoretical analysis of such copula-shaped prediction sets, proving that the  
 858 empirical copula approach achieves finite-sample validity under i.i.d. assumptions. These methods  
 859 produce tighter joint regions than the naive Cartesian product by allocating miscoverage intelligently  
 860 across coordinates, though they often rely on either simple parametric copulas or numerical search  
 to balance the marginal intervals.

861 Very recently, Dheur et al. (2025) conducted a comprehensive study of multi-output conformal meth-  
 862 ods, proposing in particular two new families of conformity scores. One uses a generative model  
 863 (e.g. an invertible normalizing flow) to transform  $Y$  into a space where conventional CP can be  
 applied coordinate-wise, and the other defines a computationally efficient scalar score by combin-

864  
 865  
 866  
 867  
 868  
 869  
 870  
 871  
 872  
 ing coordinate-wise conformal  $p$ -values (essentially summing their logarithms). Both approaches  
 attain finite-sample marginal coverage and offer improvements in conditional coverage. Notably,  
 a conceptually similar idea was introduced concurrently by Fang et al. (2025), who also leverage  
 normalizing flows to define nonconformity in the latent space. Their method (CONTRA) maps  
 high-density regions in the latent space to complex but high-coverage regions in output space, yield-  
 ing non-axis-aligned prediction sets that outperform standard hyperrectangles or ellipsoids. Despite  
 these advances, none of the above techniques exploits the full geometric structure of multivariate  
 quantiles or ranks. This gap has been filled by two concurrent works that integrate the measure-  
 transport perspective into conformal inference.

873  
 874  
 875  
 876  
 877  
 878  
 879  
 880  
 881  
 882  
 883  
 884  
 885  
 886  
 887  
 888  
 Thurin et al. (2025) introduce OT-CP, which uses the center-outward rank function of Hallin et al.  
 (2021) to define multivariate order statistics. In essence, they compute the “rank” of a test point  $y$   
 among past observations in  $\mathbb{R}^d$  via the empirical center-outward distribution (obtained by optimal  
 transport), and use the corresponding multivariate quantile level as the nonconformity score. This  
 yields a prediction region for a new  $X = x$  by including all  $y$  whose center-outward rank is above  
 a certain quantile (determined by the calibration set)—intuitively, the set of points that lie among  
 the  $(1 - \alpha)$  fraction most central (least outlying) under the conditional distribution of  $Y | X = x$ .  
 Independently, Klein et al. (2025) develop a related approach that also relies on optimal transport  
 to order multivariate outputs. They formalize the notion of distribution-free multivariate quantile  
 regions and provide finite-sample coverage guarantees for both exact and approximate transport  
 maps. These OT-based conformal methods leverage the geometry of Brenier maps (i.e. conditional  
 Monge–Ampère transports) to construct flexible, data-dependent prediction sets in  $\mathbb{R}^d$  that adapt to  
 the local distribution of  $Y | X = x$ . By exploiting the vector-quantile structure, they can achieve  
 tighter coverage with complex (even non-convex) regions while still guaranteeing the rigorous cov-  
 erage properties that make conformal prediction attractive. However, the use of optimal transport  
 maps can be computationally expensive in high dimensions, and in practice one might need to trade  
 off some statistical efficiency for tractability when estimating the transport.

889  
 890  
 891  
 892  
 893  
 894  
 895  
 896  
 897  
 898  
 899  
 900  
 901  
 Finally, an alternative direction is to explicitly optimize prediction set volume subject to cover-  
 age, rather than relying on a fixed conformity score. Braun et al. (2025) propose an optimization-  
 driven framework that learns minimum-volume covering sets for multivariate regression. In their  
 approach, the predictive model is trained jointly with a parametric prediction set (for example, an  
 adaptive norm-ball whose radius may vary with  $x$ ) to minimize the volume of the set while enforc-  
 ing coverage on the training data via a surrogate loss. This procedure effectively learns the shape  
 of the prediction region that best captures a specified proportion of the data. By conformalizing the  
 learned region (i.e. slightly expanding it to guarantee  $1 - \alpha$  coverage on a holdout set), the method  
 yields valid prediction sets that are much tighter than those from standard split-conformal methods.  
 Such approaches highlight an exciting trend of combining machine learning and conformal infer-  
 ence: rather than treating the prediction algorithm as a black box, one can optimize the model and  
 its uncertainty quantification in tandem to achieve improved efficiency (smaller, more informative  
 prediction sets) without sacrificing the finite-sample guarantees of CP.

## 902 B REMARK ON CONTINUITY OF DISTRIBUTION FUNCTION 903

904  
 905  
 906  
 907  
 908  
 909  
 The requirement that  $F_{Y|X=x}$  admit a density in Assumption 2 is stronger than needed, see (Ghosal  
 & Sen, 2022), and is not customary for conditional vector ranks. For our results, it suffices that the  
 source (reference) distribution  $F_U$  be absolutely continuous with finite second moment (e.g., uni-  
 form on  $[0, 1]^d$  or Gaussian). No density assumption on  $F_{Y|X=x}$  is required; in particular,  $F_{Y|X=x}$   
 may be discrete.

910  
 911  
 912  
 Under these conditions, for each  $x$  there exists a convex potential  $\varphi_x$  such that the Brenier map  
 $Q_{Y|X}(\cdot, x) = \nabla \varphi_x$  is defined  $F_U$ -a.e., is unique  $F_U$ -a.e., and pushes  $F_U$  forward to the conditional  
 law:

$$(Q_{Y|X}(\cdot, x))_# F_U = F_{Y|X=x}.$$

913  
 914  
 915  
 916  
 The (conditional) vector rank is given by the gradient of the convex conjugate,  $Q_{Y|X}^{-1}(\cdot, x) = \nabla \varphi_x^*$ ,  
 which is defined  $F_{Y|X=x}$ -a.e. (when  $F_{Y|X=x}$  is discrete, interpret  $Q_{Y|X}^{-1}$  as any measurable selec-  
 tion from  $\partial \varphi_x^*$ ). It transports back to the reference:

$$Q_{Y|X}^{-1}(Q_{Y|X}(u, x), x) = u \text{ for } F_U\text{-a.e. } u.$$

918 Consequently, we could work under the standing condition that  $F_U$  is absolutely continuous with  
 919 finite second moment; Theorem 1 holds verbatim with the above interpretation.  
 920

## 921 C ENTROPY-REGULARIZED NEURAL VQR

924 Let  $\mathcal{X}, \mathcal{Y}, \mathcal{U}$  be Polish spaces with Borel  $\sigma$ -algebras, and let  $m$  be the marginal law of  $X$ ,  
 925  $\nu(dx, dy) = m(dx) \nu_z(dy)$  the joint law of  $(X, Y)$ , and  $\mu(dx, du) = m(dx) \bar{\mu}(du)$  the joint law of  
 926  $(X, U)$  (where  $\bar{\mu}$  is the marginal distribution of  $U$ ). For  $\varepsilon > 0$ , the entropic-regularized *conditional*  
 927 OT problem reads (Carlier et al., 2022)

$$928 \min_{\gamma \in \mathcal{M}_+(\mathcal{X} \times \mathcal{Y} \times \mathcal{U})} \left\{ - \int u^\top y d\gamma + \varepsilon \text{KL}(\gamma \parallel \bar{\mu} \otimes \nu) \right\} \quad \text{s.t.} \quad \Pi_{X,Y} \# \gamma = \nu, \Pi_{X,U} \# \gamma = \mu. \quad (7)$$

931 This is a strictly convex problem with linear marginal constraints; KL denotes the Kullback–Leibler  
 932 divergence. (7) specializes the standard entropic OT to the conditional setting by constraining the  
 933 two  $(X, \cdot)$  marginals of  $\gamma$ .

934 **Dual formulation via Fenchel–Rockafellar.** We introduce the dual potentials  $\psi: \mathcal{X} \times \mathcal{Y} \rightarrow \mathbb{R}$  and  
 935  $\varphi: \mathcal{X} \times \mathcal{U} \rightarrow \mathbb{R}$ . A direct application of Fenchel–Rockafellar duality yields the (unconstrained) dual  
 936

$$937 \inf_{\psi, \varphi} \underbrace{\int \psi(y, x) \nu(dx, dy)}_{\text{term for } \Pi_{X,Y}} + \underbrace{\int \varphi(u, x) \mu(dx, du)}_{\text{term for } \Pi_{X,U}} \\ 938 + \varepsilon \int \int \exp \left( \frac{u^\top y - \varphi(u, x) - \psi(y, x)}{\varepsilon} \right) \nu(dx, dy) \bar{\mu}(du), \quad (8)$$

943 with zero duality gap and attainment under mild assumptions (tightness and finite entropy). The  
 944 inequality constraint of the unregularized dual is absorbed by the exponential term barrier in (8).  
 945 This could be solved using purely stochastic optimization with NN parameterization of the two dual  
 946 potentials  $\psi(y, x)$  and  $\varphi(u, x)$  similarly to what was proposed in (Genevay et al., 2016; Seguy et al.,  
 947 2018). But from a practical perspective the exponential in the loss is particularly hard to optimize  
 948 with numerical stability problems. This is why Genevay et al. (2016) proposed to remove one of the  
 949 potentials using the smooth version of the  $c$ -conjugacy detailed below.

950 **KKT/first-order conditions: soft  $c$ -conjugacy.** Assuming  $\nu$  and  $\bar{\mu}$  admit densities w.r.t. the  
 951 Lebesgue measure and differentiating the dual objective in (8) w.r.t.  $\psi$  and  $\varphi$  gives the optimality  
 952 (stationarity) conditions

$$954 \psi_\varepsilon(y, x) = \varepsilon \log \int \exp \left( \frac{u^\top y - \varphi_\varepsilon(u, x)}{\varepsilon} \right) \bar{\mu}(du), \quad (9)$$

$$956 \varphi_\varepsilon(u, x) = \varepsilon \log \int \exp \left( \frac{u^\top y - \psi_\varepsilon(y, x)}{\varepsilon} \right) \nu_x(dy), \quad (10)$$

958 which are the entropic (“soft”)  $c$ -transforms, i.e., log-partition functions of exponential families  
 959 induced by the bilinear cost  $c(u, y) = -u^\top y$ . At  $\varepsilon \downarrow 0$ , the identities (9)–(10)  $\Gamma$ -converge to the hard  
 960 Fenchel conjugacy  $\psi = \varphi^*$ , recovering the unregularized dual feasibility  $\varphi(u, x) + \psi(y, x) \geq u^\top y$   
 961 with equality on the support of the optimal plan.

962 **Reduction to a single potential (semi-dual).** Eliminating  $\psi$  in (8) via (9) yields an equivalent  
 963 unconstrained problem in  $\varphi$ :

$$965 \mathcal{U}_\varepsilon(\varphi) = \mathbb{E}_{(X,U) \sim \mu} [\varphi(U, X)] + \mathbb{E}_{(X,Y) \sim \nu} \left[ \varepsilon \log \int \exp \left( \frac{u^\top Y - \varphi(u, X)}{\varepsilon} \right) \bar{\mu}(du) \right], \quad (11)$$

968 which is precisely the regularized analogue of the conjugate-based loss in the unregularized case  
 969 (log-sum-exp replaces the sup). This problem is very interesting from an optimization perspective  
 970 because now a unique dual potential needs to be optimized and the log-sum-exp can be implemented  
 971 in a much more stable way than the exponential in the dual (8). But then the inner expectation in the  
 right part of (11) cannot be computed exactly, which we discuss next.

972 **Gibbs conditionals and gradients.** Define the Gibbs conditional density (a.k.a. Schrödinger bridge  
 973 “posterior”)

$$974 \quad 975 \quad \pi_\varphi(du \mid y, x) \propto \exp\left(\frac{u^\top y - \varphi(u, x)}{\varepsilon}\right) \bar{\mu}(du).$$

976 As in the not regularized case, we parameterize the potential  $\varphi_\varepsilon$  with a neural network. We denote  
 977 by  $\theta$  the parameters (weights) of this network. Using the log-partition derivative identity, we get that  
 978  $\nabla_\theta \mathcal{U}_\varepsilon(\varphi_\theta)$  admits the “positive minus negative phase” form

$$979 \quad 980 \quad \nabla_\theta \mathcal{U}_\varepsilon(\varphi_\theta) = \mathbb{E}_{(X, U) \sim \mu} [\nabla_\theta \varphi_\theta(X, U)] - \mathbb{E}_{(X, Y) \sim \nu} \mathbb{E}_{U \sim \pi_{\varphi_\theta}(\cdot \mid Y, X)} [\nabla_\theta \varphi_\theta(X, U)], \quad (12)$$

981 obtained by differentiating the log-partition in (11). In practice, the inner expectation is estimated  
 982 by Monte Carlo with  $U$  drawn either from  $\pi_{\varphi_\theta}(\cdot \mid Y, X)$  or via importance sampling from  $\bar{\mu}$  with  
 983 the usual exponential weights.

984 **Quantile and rank maps under entropic regularization.** If  $u \mapsto \varphi_\varepsilon(u, x)$  is (strongly) convex  
 985 and smooth, the regularized analogues of the conditional vector quantile and rank are

$$986 \quad Q_{Y|X}^{(\varepsilon)}(u, x) := \nabla_u \varphi_\varepsilon(u, x), \quad (13)$$

$$987 \quad (Q_{Y|X}^{(\varepsilon)})^{-1}(y, x) := \nabla_y \psi_\varepsilon(y, x) = \mathbb{E}_{U \sim \pi_{\varphi_\varepsilon}(\cdot \mid y, x)} [U], \quad (14)$$

988 where the last identity follows by differentiating (9). Equations (13)–(14) are the entropic counter-  
 989 parts of the unregularized identities and reduce to them as  $\varepsilon \downarrow 0$ .

990 **Limit  $\varepsilon \downarrow 0$ .** As  $\varepsilon \rightarrow 0$ ,  $\varepsilon \log \int \exp((\cdot)/\varepsilon) \rightarrow \sup(\cdot)$ , so

$$991 \quad \mathcal{U}_\varepsilon(\varphi) \xrightarrow[\varepsilon \downarrow 0]{} \mathbb{E}_\mu[\varphi(X, U)] + \mathbb{E}_\nu[\varphi^*(X, Y)],$$

992 recovering the unregularized loss with the hard Fenchel conjugate and the transition from the con-  
 993 strained dual (inequality) to the unconstrained conjugate form. In the same limit,  $\pi_\varphi(\cdot \mid y, x)$   
 994 concentrates on the (possibly set-valued) argmax of  $u \mapsto u^\top y - \varphi(u, x)$ , and (13)–(14) converge to  
 995 the OT maps of the unregularized problem.

## 1001 D CONDITIONAL CONVEX POTENTIAL FLOWS

1002 **Conditional (partially convex) construction.** Given covariates  $x \in \mathcal{X}$ , we model the conditional  
 1003 transport by a *partially* input-convex potential

$$1004 \quad \varphi: \mathbb{R}^d \times \mathcal{X} \rightarrow \mathbb{R}, \quad u \mapsto \varphi(u; x) \text{ convex (strongly convex) for each fixed } x,$$

1005 and define the *conditional convex potential flow* (a.k.a. *partially convex potential flow*)

$$1006 \quad Q_{Y|X}(u, x) := \nabla_u \varphi(u; x), \quad U \sim f_U \rightsquigarrow Y \mid X = x \text{ via } Y = Q_{Y|X}(U, x).$$

1007 Under absolute continuity of  $f_{Y|X}(\cdot \mid x)$  (see Assumption 2), the conditional *rank map* (inverse  
 1008 quantile) exists and is the gradient of the conjugate:

$$1009 \quad Q_{Y|X}^{-1}(y, x) = \nabla_y \varphi^*(y; x),$$

1010 and the two maps are inverses a.e. (in  $u$  and  $y$ ) for each  $x$ . For any  $(y, x)$  such that the inverse is  
 1011 well defined.

$$1012 \quad f_{Y|X}(y \mid x) = f_U(Q_{Y|X}^{-1}(y, x)) \det \left[ \nabla_y Q_{Y|X}^{-1}(y, x) \right]. \quad (15)$$

1013 Equivalently, writing  $y = \nabla_u \varphi(u; x)$  with  $u = Q_{Y|X}^{-1}(y, x)$ ,

$$1014 \quad \log f_{Y|X}(y \mid x) = \log f_U(u) - \log \det [\nabla_{uu}^2 \varphi(u; x)].$$

1015 Thus maximum likelihood amounts to estimating  $\varphi$  so as to match the pullback  $Q_{Y|X}^{-1}(Y, X)$  to  
 1016 the prior  $f_U$ , while penalizing the local volume change through the (log) Hessian determinant. In  
 1017 practice, the log-determinant and its gradients can be computed with Hessian–vector products, using  
 1018 stochastic Lanczos/trace estimators and conjugate-gradient solves, yielding unbiased  $O(1)$ –memory  
 1019 estimators that scale to high dimension.

1026

**Inversion and sampling.** For any  $(y, x)$ , inversion is a convex program:

1027

$$Q_{Y|X}^{-1}(y, x) = \arg \min_{u \in \mathbb{R}^d} \varphi(u; x) - y^\top u,$$

1029

1030 whose optimality condition  $\nabla_u \varphi(u; x) = y$  recovers the required  $u$ . This is precisely the evaluation  
 1031 of  $\nabla_y \varphi^*(y; x)$  and can be carried out with off-the-shelf smooth convex solvers; batched inversions  
 1032 reduce to minimizing summed potentials over independent inputs.

1033

1034 Under mild regularity (convex support and densities), there exists a measurable conditional vector  
 1035 quantile  $Q_{Y|X}$  that is the gradient (in  $u$ ) of a convex potential and pushes  $U$  to  $Y | X = x$ ; the  
 1036 inverse rank is the gradient (in  $y$ ) of the conjugate, and  $Q_{Y|X}$  solves the  $W_2$  OT problem condition-  
 1037 ally on  $x$ . Hence the partially convex potential flow inherits both identifiability (a.e. uniqueness) and  
 1038 optimality properties in the conditional setting.

1039

1040 **Parameterization.** We instantiate  $\varphi(\cdot; x)$  with partially input-convex networks (e.g.,  
 1041 PICNN/PISCNN) to guarantee convexity in  $u$  while conditioning on  $x$ , and add a quadratic  
 1042  $\frac{\alpha}{2} \|u\|^2$  when strong convexity is desired. Universality of ICNNs in approximating convex functions  
 1043 then lifts to distributional universality of the induced conditional flows and convergence to the  
 1044 conditional OT maps.

1045

## E NUMERICAL IMPLEMENTATION

1046

1047 This section details architectures, solvers, and training procedures for our neural vector quantile  
 1048 regression (VQR) models, both in the unregularized and entropic-regularized settings, together  
 1049 with the amortized conjugate prediction used to accelerate training. We emphasize implementation  
 1050 choices that preserve convexity/monotonicity and lead to stable gradients, and we provide concrete  
 1051 defaults for reproducibility.

1052

1053 **Notation recap.** We parameterize a *conditional convex potential*  $\varphi_\theta : \mathcal{U} \times \mathcal{X} \rightarrow \mathbb{R}$  that is convex in  
 1054  $u \in \mathcal{U} \subset \mathbb{R}^{d_y}$  for each fixed  $x \in \mathcal{X}$ . The conditional vector quantile and rank maps are the gradients  
 1055 of  $\varphi_\theta$  and its Fenchel conjugate  $\varphi_\theta^*$  (see Section 2):

1056

$$Q_{Y|X}(u, x) = \nabla_u \varphi_\theta(u, x), \quad Q_{Y|X}^{-1}(y, x) = \nabla_y \varphi_\theta^*(y, x).$$

1057

1058 The conjugate evaluation at  $(y, x)$  solves  $\hat{u}_\theta(y, x) \in \arg \max_{u \in \mathcal{U}} \{u^\top y - \varphi_\theta(u, x)\}$ . By Danskin’s  
 1059 theorem, gradients w.r.t.  $\theta$  do *not* require differentiating through  $\hat{u}_\theta$ ; only  $\nabla_\theta \varphi_\theta$  at  $u = \hat{u}_\theta$  is needed.

1060

### E.1 PARTIALLY INPUT CONVEX NEURAL NETWORKS (PICNN)

1061

1062 We instantiate  $\varphi_\theta$  as a *Partially Input Convex Neural Networks* (PICNNs; Amos et al., 2017) that is  
 1063 convex in  $u$  and conditions on  $x$ :

1064

$$(u, x) \mapsto \varphi_\theta(u, x) = \text{PICNN}(u, x; \theta),$$

1065

1066 with layerwise updates

1067

$$c_{i+1} = \tilde{g}_i(\tilde{W}_i c_i + \tilde{b}_i),$$

1069

$$z_{i+1} = g_i\left(W_i^{(z)}(z_i \circ [W_i^{(zc)} c_i + b_i^{(z)}]_+) + W_i^{(u)}[u \circ (W_i^{(uc)} c_i + b_i^{(u)})] + W_i^{(c)} c_i + b_i\right),$$

1070

1071 and output  $\varphi_\theta(u, x) = z_K$ . We initialize  $c_0 = x, z_0 = 0$ . Here  $\circ$  denotes the element-wise product.  
 1072 We enforce elementwise nonnegativity of  $W_i^{(z)}$  and  $[ \cdot ]_+$  via a Softplus reparameterization:

1073

1074

$$W_i^{(z)} = \log\left(1 + \exp\left(\tilde{W}_i^{(z)}\right)\right), \quad \tilde{W}_i^{(z)} \in \mathbb{R}^{p \times k}, \quad (16)$$

1075

1076

$$[W_i^{(zc)} c_i + b_i^{(z)}]_+ = \log\left(1 + \exp\left(W_i^{(zc)} c_i + b_i^{(z)}\right)\right). \quad (17)$$

1077

1078

1079 We use convex, non-decreasing activations for  $g_i, \tilde{g}_i$ , which guarantees convexity in  $u$  while retaining  
 1080 expressive power. We optionally add a quadratic term  $\frac{\alpha}{2} \|u\|_2^2$  (trainable  $\alpha \geq 0$ ) to obtain strong  
 1081 convexity, improving stability of the inner argmax (Amos et al., 2017, Proposition 2). We choose

1080 Softplus as non-linearity for  $g_i$  and ELU as non-linearity for  $c_i$ . Following Huang et al. (2021)  
 1081 we utilize activation normalization ActNorm layers (Kingma & Dhariwal, 2018) before applying  
 1082 the  $g_i$  non-linearity. Final architecture of one iterate hence becomes.  
 1083

$$1084 \quad c_{i+1} = \text{ELU}(\tilde{W}_i c_i + \tilde{b}_i), \\ 1085 \quad z_{i+1} = \text{Softplus}\left(\text{ActNorm}\left(W_i^{(z)}\left(z_i \circ \left[W_i^{(zc)} c_i + b_i^{(z)}\right]_+\right) + W_i^{(u)}\left(u \circ \left[W_i^{(uc)} c_i + b_i^{(u)}\right]\right) + W_i^{(c)} c_i + b_i\right)\right), \\ 1086 \\ 1087 \\ 1088$$

### 1089 Practical tips (PICNN).

1090 (i) Normalize  $u$  and  $y$  scales (e.g. standardization) to ease optimization;  
 1091 (ii) We use weight decay on  $\theta$  and (if enabled) a small ridge  $\alpha$  to avoid flat directions;  
 1092 (iii) We clip gradients of  $\varphi_\theta$  to bound the Lipschitz constant of  $u \mapsto \nabla_u \varphi_\theta(u, x)$ .  
 1093

## 1094 E.2 PARTIALLY INPUT STRONGLY CONVEX NEURAL NETWORK (PISCNN)

$$1096 \quad \text{PISCNN}(u, x) = \text{PICNN}(u, x) + \frac{\alpha}{2} \|u\|_2^2,$$

1097 which is strongly convex in  $u$  and yields a *strictly concave* inner objective  $u \mapsto u^\top y - \varphi_\theta(u, x)$ ,  
 1098 ensuring a unique maximizer  $\hat{u}_\theta(y, x)$  and faster, more reliable inner solves. We treat  $\alpha$  as positive  
 1099 scalar parametrized by  $e^w$ , where  $w$  is a trainable parameter. In all our implementations, enabling  
 1100  $\alpha > 0$  eliminated numerical non-uniqueness in the conjugate and reduced inner iterations.  
 1101

## 1102 E.3 COMPUTING THE CONJUGATE: INNER MAXIMIZATION

1103 Given  $(y, x)$  and current  $\theta$ , we compute

$$1104 \quad \hat{u}_\theta(y, x) \in \arg \max_{u \in \mathcal{U}} J_\theta(u; y, x), \quad J_\theta(u; y, x) := u^\top y - \varphi_\theta(u, x).$$

1105 **Gradient and Hessian.**  $\nabla_u J_\theta(u; y, x) = y - \nabla_u \varphi_\theta(u, x)$  and  $\nabla_{uu}^2 J_\theta(u; y, x) = -\nabla_{uu}^2 \varphi_\theta(u, x) \preceq 0$ . With PISCNN,  $\nabla_{uu}^2 \varphi_\theta(u, x) \succeq \alpha I$  ensures strong concavity.  
 1106

1107 **Solver.** We minimize  $-J_\theta$  with L-BFGS. For stability:

- 1108 **Warm start.** We initialize the solver from amortized predictor  $\tilde{u}_\theta(y, x)$  when available (see  
 1109 Section E.4) or otherwise initialize it at  $u \sim F_U$ .
- 1110 **Domain handling.** If  $\mathcal{U}$  is a ball/hypercube, we project the solution after each step:  $u \leftarrow \Pi_{\mathcal{U}}(u)$ .
- 1111 **Stopping.** Terminate when  $\|\nabla_u J_\theta\| \leq \varepsilon_{\text{norm}}$ ,  $\|J_\theta(u_i; y, x) - J_\theta(u_{i+1}; y, x)\| \leq \varepsilon_{\text{obj}}$  or after  
 1112  $K_{\text{max}}$  steps (defaults:  $\varepsilon_{\text{norm}} = 10^{-7}$ ,  $\varepsilon_{\text{obj}} = 10^{-7}$ ,  $K_{\text{max}} = 1000$ ).  
 1113

## 1114 E.4 AMORTIZED CONJUGATE PREDICTION

1115 To avoid expensive inner solves at every iteration, we learn a differentiable predictor  $\tilde{u}_\theta : \mathcal{Y} \times$   
 1116  $\mathcal{X} \rightarrow \mathcal{U}$  that approximates  $\hat{u}_\theta(y, x)$  and serves as a warm start for L-BFGS solver. We parametrize  
 1117  $\tilde{u}_\theta(y, x)$  as feed forward neural network with a residual skip connection to encourage identity at  
 1118 initialization

$$1119 \quad \tilde{u}_\theta(y, x) = \text{MLP}_\theta\left(\begin{bmatrix} y \\ x \end{bmatrix}\right) + W_y y + b_y.$$

1120 **Training losses.** Several loss functions have been explored in the literature. Objective-  
 1121 based losses (Dam et al., 2019; Amos, 2023) optimize the network to predict the maximum  
 1122 of the conjugate by maximizing  $\mathcal{V}_{\text{obj}} = \mathbb{E}_{(Y, X) \sim F_{YX}} [J_\theta(\tilde{u}_\theta; y, x)]$ . Alternatively, one may  
 1123 enforce the first-order condition  $\nabla_u \varphi_\theta(u, x)|_{u=\tilde{u}_\theta(y, x)} \approx y$  via the residual loss  $\mathcal{V}_{\text{res}}(\vartheta) =$   
 1124  $\mathbb{E}_{(Y, X) \sim F_{YX}} [\|\nabla_u \varphi_\theta(u, x)|_{u=\tilde{u}_\theta(y, x)} - y\|_2^2]$ . If the true conjugate  $\tilde{u}_{\varphi_\theta(\cdot, x)}(y)$  (4) is available, one  
 1125 can regress directly with  $\mathcal{V}_{\tilde{u}} = \mathbb{E}_{(Y, X) \sim F_{YX}} [\|\tilde{u}_\theta(y, x) - \tilde{u}_{\varphi_\theta(\cdot, x)}(y)\|_2^2]$ . In practice, we observe  
 1126 no major differences between these approaches and therefore adopt  $\mathcal{V}_{\tilde{u}}$  as our loss of choice (see  
 1127 Algorithm 2).  
 1128

1134 E 5 ENTROPIC-REGULARIZED SEMI-DUAL

1135

1136 When using the entropic semi-dual  $U_\varepsilon(\varphi)$  (see Appendix C), we replace the hard conjugate with a  
 1137 log-sum-exp:

1138

$$U_\varepsilon(\varphi_\theta) = \mathbb{E}_{(X,U)}[\varphi_\theta(U, X)] + \mathbb{E}_{(X,Y)} \left[ \varepsilon \log \mathbb{E}_{U \sim F_U} \exp \left( \frac{U^\top Y - \varphi_\theta(U, X)}{\varepsilon} \right) \right].$$

1141

**1142 Monte Carlo and stability.** We approximate the inner expectation with  $m$  i.i.d. samples  $U_j \sim$   
**1143**  $F_U$ , using a numerically stable log-sum-exp with 64-bit accumulation. We found  $m \in [512, 1024]$   
**1144** adequate on our benchmarks, and we re-sample the  $U_j$  each iteration. In the  $\varepsilon \downarrow 0$  limit, this recovers  
**1145** the unregularized loss. We intentionally set high amount of samples for dual objective estimation to  
**1146** avoid effects related to high bias of logsumexp estimator.

1147 **Gradients.** The gradient has a positive-minus-negative phase form using the Gibbs weights (see  
1148 Appendix C and equation (12)), which we implement without storing the full batch  $\times m$  tensor by  
1149 streaming accumulation.

1150

1151 E.6 TRAINING LOOPS AND ALGORITHMS

1152

1153 We describe three loops: (i) Neural Vector Quantile Regression without amortization Algorithm 1,  
 1154 (ii) Amortized Vector Quantile Regression Algorithm 2, and (iii) Entropic Semi-dual Algorithm 3.  
 1155 All use AdamW (initial LR of  $10^{-2}$ , weight decay  $10^{-4}$ ) with cosine annealing (LR decaying to  
 1156 0), batch size 1024, and gradient clipping at 10. We sample  $U \sim F_U$  as standard Gaussian unless  
 1157 otherwise noted. See Appendix H.2 for dataset-specific details. We use warm restarts for amortized  
 1158 network, restarting the learning rate to  $10^{-2}$  each 10 epochs.

1159

---

**Algorithm 1** Neural Vector Quantile Regression Training (C-NQR)

```

1: Input: dataset  $\{(x_i, y_i)\}_{i=1}^n$ , PICNN  $\varphi_\theta: \mathcal{U} \times \mathcal{X} \rightarrow \mathbb{R}$ 
2: Sample mini-batch  $\mathcal{B} \subset \{1, \dots, n\}$ 
3: Initialize  $\mathcal{V}_\varphi \leftarrow 0$ 
4: for each  $i \in \mathcal{B}$  do
5:    $\check{u}_i \leftarrow \arg \max_{u \in \mathcal{U}} J_{\varphi_\theta(\cdot, x_i)}(u, y_i)$  ▷ Run L-BFGS for each  $y_i$  starting at  $u = 0$ 
6:    $\hat{\psi}_i(\theta) \leftarrow J_{\varphi_\theta(\cdot, x_i)}(\check{u}_i, y_i)$ 
7:   Sample  $u_i \sim \mathcal{N}(0, I_d)$ 
8:    $\hat{\varphi}_i(\theta) \leftarrow \varphi_\theta(u_i, x_i)$ 
9:    $\hat{\mathcal{V}}_\varphi(\theta) \leftarrow \hat{\mathcal{V}}_\varphi(\theta) + \hat{\psi}_i(\theta) + \hat{\varphi}_i(\theta)$ 
10: end for
11: Compute  $\nabla_\theta \frac{1}{|\mathcal{B}|} \hat{\mathcal{V}}_\varphi(\theta)$  ▷ Do not propagate gradients through  $\check{u}$ 
12: Update  $\theta$  with Adam

```

1173

## E 7 CONFORMAL METHODS IMPLEMENTATION

1176 Here, we provide a detailed description of our implementation of the methods introduced in Sec-  
 1177 tion 4. For all proposed approaches, we start with an estimate  $\widehat{Q}_{Y|X}^{-1}(y, x)$  that we obtain using a  
 1178 training set  $\mathcal{D}_{\text{train}}$ . All conformal methods operate on a separate held-out calibration set  $\mathcal{D}_{\text{cal}}$ . Since  
 1179 we need to replicate our uncertainty estimation experiments for multiple splits and datasets, we use  
 1180 the Amortized Neural Vector Quantile Regression version of our algorithm.

**Split Conformal Prediction with Monge-Kantorovich ranks.** An instance of classical split conformal prediction using a score derived from our vector quantile regressor.

**1184** **Fixed re-ranking.** To account for the misspecification of  $\widehat{Q}_{Y|X}^{-1}(y, x)$  we introduce an intermediate  
**1185** re-ranking of  $U_i$ . We follow the approach of Thurin et al. (2025), but instead of a separate base  
**1186** model, we directly use our estimate:  $S_i = U_i = \widehat{Q}_{Y|X}^{-1}(Y_i, X_i) \in \mathbb{R}^{d_y}$ . We divide our calibration  
**1187** set into two parts; the first part is used to estimate an OT map  $\mathbf{R}: \mathcal{U} \rightarrow \mathcal{U}'$  and the second part is

---

1206 **Algorithm 3** Entropic semi-dual training (EC-NQR)  
1207 1: **Input:** dataset  $\{(x_i, y_i)\}_{i=1}^n$ , PICNN  $\varphi_\theta: \mathcal{U} \times \mathcal{X} \rightarrow \mathbb{R}$   
1208 2: Sample mini-batch  $\mathcal{B} \subset \{1, \dots, n\}$   
1209 3: initialize  $\mathcal{L}_\varphi \leftarrow 0$   
1210 4: Sample i.i.d.  $u_{ij} \sim F_U$   
1211 5: **for** each  $i \in \mathcal{B}$  **do**  
1212 6:      $\hat{\psi}_i(\theta) \leftarrow \epsilon \log \sum_{j=1}^m \exp \left( \frac{u_{ij}^T y_i - \varphi_\theta(u_{ij}, x_i)}{\epsilon} \right)$   $\triangleright \epsilon \in [10^{-3}, 10^{-1}]$   
1213 7:     Sample  $u_i \sim F_U$   
1214 8:      $\hat{\varphi}_i(\theta) \leftarrow \varphi_\theta(u_i, x_i)$ ;  
1215 9:      $\mathcal{L}_\varphi(\theta) \leftarrow \mathcal{L}_\varphi(\theta) + \hat{\psi}_i(\theta) + \hat{\varphi}_i(\theta)$   
1216 10: **end for**  
1217 11: Compute  $\nabla_\theta \frac{1}{|\mathcal{B}|} \mathcal{L}_\varphi(\theta)$   
1218 12: Update  $\theta$  with Adam

---

---

1222   **Algorithm 4** Pull-back split conformal prediction

1223

1224   1: **Input:** dataset  $\mathcal{D}_{\text{cal}} = \{(X_i, Y_i)\}_{i=1}^n$ , trained model  $\hat{Q}_{Y|X}^{-1}(y, x)$ , a new test point  $(X_{\text{test}}, Y_{\text{test}})$

1225       and the desired nominal miscoverage level  $\alpha$

1226   2: **for** each  $i \in \{1, \dots, n\}$  **do**

1227       3:      $U_i \leftarrow \hat{Q}_{Y|X}^{-1}(Y_i, X_i)$

1228       4:      $S_i \leftarrow \|U_i\|$

1229       5: **end for**

1230       6:  $\rho_{1-\alpha} \leftarrow \lceil (n+1)(1-\alpha) \rceil$ -th largest  $S_i$

1231       7:  $\hat{\mathcal{C}}_{\alpha}^{\text{pb}}(X_{\text{test}}) \leftarrow \left\{ y: \|\hat{Q}_{Y|X}^{-1}(y, X_{\text{test}})\| \leq \rho_{1-\alpha} \right\}$

1232

---

1236 used to conformalize the result. In our experiments, we follow the original authors' approach and  
 1237 use  $\mathcal{U}' = U(S^{d_y-1})$  - uniform distribution on the unit ball. To evaluate the map  $\hat{R}$  on the new point,  
 1238 we map it to the corresponding closest point from the first calibration part.  
 1239

1239  
 1240 We use the code of Thurin et al. (2025) to estimate  $\widehat{\mathbf{R}}$  (we divide the original calibration set into  
 1241 two equal parts). This implementation uses the renowned POT library (Flamary et al., 2021), which  
 provides efficient implementations of the various optimal transport techniques.

---

1242                   **Algorithm 5** Re-ranked pull-back split conformal prediction

---

1243                   1: **Input:** dataset  $\mathcal{D}_{\text{cal}} = \{(X_i, Y_i)\}_{i=1}^{n=n_1+n_2}$ , trained model  $\hat{Q}_{Y|X}^{-1}(y, x)$ , a new test point  
1244                    $(X_{\text{test}}, Y_{\text{test}})$  and the desired nominal miscoverage level  $\alpha$

1245                   2: **for** each  $i \in \{1, \dots, n_1\}$  **do**

1246                   3:      $U_i \leftarrow \hat{Q}_{Y|X}^{-1}(Y_i, X_i)$

1247                   4: **end for**

1248                   5: Estimate  $\hat{\mathbf{R}}$  using sample  $(\{U_i\}_{i=1}^{n_1}, \{U'_i\}_{i=1}^{n_1})$                    ▷  $\{U'_i\}_{i=1}^{n_1}$  - reference sample from  $\mathcal{U}'$

1249                   6: **for** each  $j \in \{1, \dots, n_2\}$  **do**

1250                   7:      $S_j \leftarrow \left\| \hat{\mathbf{R}} \left( \hat{Q}_{Y|X}^{-1}(Y_j, X_j) \right) \right\|$

1251                   8: **end for**

1252                   9:  $\rho_{1-\alpha} \leftarrow \lceil (n_2 + 1)(1 - \alpha) \rceil$ -th largest  $S_j$

1253                   10:  $\hat{\mathcal{C}}_{\alpha}^{\text{rpb}}(X_{\text{test}}) \leftarrow \left\{ y: \left\| \hat{\mathbf{R}} \left( \hat{Q}_{Y|X}^{-1}(y, X_{\text{test}}) \right) \right\| \leq \rho_{1-\alpha} \right\}$

---

1258                   Table 3: Model hyperparameters for different datasets.

1259 <b>Dataset(s)</b>	1260 <b>Layer width</b>	1261 <b>Layer depth</b>	1262 <b>Batch size</b>
1263                   bio	12	4	512
1264                   blog	16	4	512
1265                   sgemm	46	4	8192
1266                   scm20d	10	1	2048
1267 <i>Banana, Convex Banana, Star, Convex Star</i>	18	8	256
1268 <i>Glasses, Convex Glasses, Funnel</i>	18	8	256

## 1268                   E.8 HYPERPARAMETERS AND DEFAULT CONFIGURATION

- 1269                   • **Network sizes.** We typically use around 10% of available data as parameters scale. See  
1270                   Appendix E.8 for details.
- 1271                   • **Optimization.** AdamW (LR  $10^{-2}$ , weight decay  $10^{-4}$ ). We use cosine warm restart for  
1272                   amortization network every 5k–10k steps; We clip gradients at 1.0.
- 1273                   • **Inner solver.** L-BFGS with Wolfe line search,  $K_{\text{max}} = 50$  (amortized) or 100 (no amorti-  
1274                   zation); tolerance  $10^{-5}$ ; domain projection when  $\mathcal{U}$  is bounded.
- 1275                   • **Amortizer.** Amortization network copies the potential network architecture in all our ex-  
1276                   periments.
- 1277                   • **Entropic.** In all our experiments we fix  $\varepsilon = 0.001$ ;  $m = 1024$  Monte Carlo samples per  
1278                    $(x, y)$ .

1281                   These defaults matched the settings used across Section 6.1 and Section 6.2 (metrics and datasets).

## 1284                   F DEFERRED CONTENT FOR CONFORMAL PREDICTION

1286                   We now proceed to provide the deferred content from Section 4. We start by restating Theorem 3  
1287                   and its proof. Then, we showcase a setting where the assumptions of Theorem 3 are met. Finally, we  
1288                   explain how the OT maps  $Q_{Y|X}$  and  $Q_{Y|X}^{-1}$  may be used to construct conformal sets using density  
1289                   estimation.1290                   **Theorem 4** (Volume–optimality of pullback balls under radiality). *Fix  $x \in \mathcal{X}$  and reference dis-  
1291                   tribution  $F_{\mathcal{U}}(u) = \phi(\|u\|)$  for a continuous  $\phi: [0, \infty) \rightarrow (0, \infty)$  on  $\mathcal{U}$ , under the assumptions of  
1292                   Theorem 1, let  $Q_{Y|X}$  and  $Q_{Y|X}^{-1}$  be the vector quantile and multivariate rank functions. Assume that  
1293                   there exists  $j_x$  such that for all  $y$  in the support of  $F_{Y|X}$ , it holds*

1294                   
$$\det \left[ \nabla_y Q_{Y|X}^{-1}(y, x) \right] = j_x \left( \|Q_{Y|X}^{-1}(y, x)\| \right),$$

1296 and the function  $r \mapsto \phi(r) j_x(r)$  is strictly decreasing. Let  $r_\alpha > 0$  be the unique radius satisfying  
1297  $\mu(B_{r_\alpha}) = 1 - \alpha$ , where  $\mu$  is the law corresponding to  $F_U$  and  $B_r = \{u: \|u\| \leq r\}$ . Define  
1298 the pullback ball  $\mathcal{C}_\alpha^{\text{pb}}(x) := \{y: \|Q_{Y|X}^{-1}(y, x)\| \leq r_\alpha\}$ . Then,  $\mathcal{C}_\alpha^{\text{pb}}(x)$  minimizes Lebesgue volume  
1299 among all sets with  $x$ -conditional coverage of at least  $1 - \alpha$ , i.e., for every measurable  $A \subset \mathcal{Y}_x$  with  
1300  $\mathbb{P}\{Y \in A \mid X = x\} \geq 1 - \alpha$ ,  $\text{Vol}(\mathcal{C}_\alpha^{\text{pb}}(x)) \leq \text{Vol}(A)$ .  
1301

1302 *Proof.* Let  $S_x(\cdot) = Q_{Y|X}^{-1}(\cdot)$ . Then, by the change of variables formula for densities:

$$1305 f_{Y|X}(y, x) = f_U(S_x(y)) |\det[\nabla_y S_x(y)]|.$$

1306 Using the assumption that  $f_U(u) = \phi(\|u\|)$  and  $\det[\nabla_y S_x(y)] = j_x(\|S_x(y)\|)$ . Using Carlier  
1307 et al. (2016, Corollary 2.1), we note that  $S_x$  is  $C^1$  and the derivative of a convex function. Thus, it  
1308 holds that  $y \rightarrow \det[\nabla_y S_x(y)]$  is positive and continuous, which allow for dropping absolute value  
1309 to recover

$$1311 f_{Y|X}(y, x) = \phi(\|S_x(y)\|) j_x(\|S_x(y)\|) =: h_x(\|S_x(y)\|).$$

1312 As both  $\phi$  and  $y \rightarrow j_x(\|S_x(y)\|)$  are continuous,  $h_x$  is a strictly decreasing continuous invertible  
1313 function. Hence,  $f_{Y|X}(\cdot, x)$  is a non-increasing function of the  $U$ -radius  $\|S_x(y)\|$  and its superlevel  
1314 sets are pullbacks of Euclidean balls: for each  $t > 0$  there exists  $r(t) \geq 0$  such that

$$1315 \{y: f_{Y|X}(y, x) \geq t\} = \{y: h_x(\|S_x(y)\|) \geq t\} = \{y: \|S_x(y)\| \leq r(t)\}.$$

1317 We first record the probability identity. For any Borel  $A \subset \mathcal{Y}_x$ ,

$$1319 \mathbb{P}\{Y \in A \mid X = x\} = \mu(\{S_x(y) \mid y \in A\}).$$

1320 Therefore  $\mathbb{P}\{Y \in \mathcal{C}_\alpha^{\star}(x) \mid X = x\} = \mu(B_{r_\alpha}) = 1 - \alpha$ .

1322 For volume optimality, note that since  $f_{Y|X}(y, x) = h_x(\|S_x(y)\|)$  with  $h_x$  non-increasing, ev-  
1323 ery HPD superlevel set  $\{y: f_{Y|X}(y, x) \geq t\}$  is (almost surely) a pullback set of the form  
1324  $\{y: \|S_x(y)\| \leq r(t)\}$ . Choosing  $t_\alpha$  so that  $\mathbb{P}\{Y \in \{f_{Y|X}(\cdot, x) \geq t_\alpha\} \mid X = x\} = 1 - \alpha$  forces  
1325  $\mu(B_{r(t_\alpha)}) = 1 - \alpha$ , hence  $r(t_\alpha) = r_\alpha$  and the HPD set equals  $\mathcal{C}_\alpha^{\text{pb}}(x)$ .  $\square$

1327 *Remark 3* (Examples satisfying assumptions of Theorem 3). Fix  $x$ . Let the reference be spherical  
1328 with radial, strictly decreasing continuous density  $f_U(u) = \phi(\|u\|)$ . Suppose  $Y \mid X = x$  is elliptical  
1329 with location  $m(x)$  and a positive definite scatter matrix  $\Sigma(x)$  whose whitened density uses the same  
1330 radial generator as  $U$ , i.e.,

$$1331 f_{Y|X=x}(y) \propto \phi\left(\left\|\Sigma(x)^{-1/2}(y - m(x))\right\|\right).$$

1333 Then the map  $S_x(y) = \Sigma(x)^{-1/2}(y - m(x))$  and  $\det[\nabla_y S_x(y)] \equiv \det(\Sigma(x)^{-1/2})$ . This setting  
1334 includes the Gaussian case by taking  $\phi(r) \propto e^{-r^2/2}$ .

1336 To show that  $S_x$  is indeed the optimal transport map, note that  $S_x$  is the gradient of convex quadratic  
1337 function. Thus, it satisfies the Brenier optimal transport conditions for the Euclidean quadratic cost  
1338 and, by Knott–Smith optimality criterion, it is the vector quantile function (Knott & Smith, 1984).

1339 **Conformal HDP Sets using OT Parameterization.** While the CQR-like construction in Section 4  
1340 is robust and simple, its prediction sets are images of Euclidean spheres and thus topologically  
1341 connected since, under Assumption 1 and Assumption 2,  $Q_{Y|X}^{-1}$  is continuous by Carlier et al. (2016,  
1342 Corollary 2.1). This can be inefficient if for some  $x \in \mathcal{X}$ , the true conditional distribution  $F_{Y|X=x}$   
1343 is multimodal, for example a Gaussian mixture. To solve this problem, it is possible to construct  
1344 prediction sets using the level sets of an estimated conditional density, which can naturally form  
1345 disconnected regions.

1346 This approach utilizes the change-of-variables formula and leveraging  $\widehat{Q}_{Y|X}^{-1}$  to recover the plug-in  
1347 conditional density estimator

$$1348 \widehat{p}(y \mid x) = f_U(\widehat{Q}_{Y|X}^{-1}(y, x)) \det[\nabla_y \widehat{Q}_{Y|X}^{-1}(y, x)].$$

This estimator can then be used to define conformity scores. For each point  $(Y_i, X_i)$  in the calibration set  $\mathcal{D}_{\text{cal}}$  we calculate the score  $s_i = \hat{p}(Y_i \mid X_i)$ . The prediction set for a new point  $X_{\text{test}}$  is the superlevel set of this estimated density, where the level is calibrated to ensure coverage. If  $s_{(1)} \leq \dots \leq s_{(n)}$  are the ordered scores from the calibration set, we set the threshold  $\tau = s_{(\lfloor (n+1)\alpha \rfloor)}$ . Then, the HPD-style prediction region is given by:

$$\mathcal{C}_\alpha^{\text{hpd}}(x) = \{y \in \mathcal{Y} : \hat{p}(y \mid x) \geq \tau\}.$$

By standard arguments, this set fulfills the marginal coverage guarantee  $\mathbb{P}_{(Y,X) \sim F_{YX}}(Y \in \mathcal{C}_\alpha^{\text{hpd}}(X)) \geq 1 - \alpha$ . Crucially, if the learned map  $\hat{Q}_{Y|X}^{-1}$  recovers the true rank map, then  $\hat{p}(\cdot \mid x)$  recovers the true conditional density, and the resulting prediction set is exactly the true HPD region.

**Related density-based approaches.** The idea of using density estimation to construct conformal sets has been exploited in recent related works. For example, in the setting with  $\mathcal{Y} \subseteq \mathbb{R}$ , *CD-split* partition  $\mathcal{X}$  into multiple splits, leverage a conditional density estimator  $\hat{f}(y \mid x)$ , and perform conformal calibration in split-wise manner to improve conditional coverage (Izbicki et al., 2022). Furthermore, also in the setting with  $\mathcal{Y} \subseteq \mathbb{R}$ , *SPICE* learns a neural conditional density via deep splines and uses negative log-density/HPD scores to construct the conformal sets (Diamant et al., 2024).

*Remark 4.* To construct conformal sets using density estimation, the estimator of  $\hat{p}(y \mid x)$  requires the Jacobian of  $\hat{Q}_{Y|X}^{-1}$ . Even if  $\hat{Q}_{Y|X}^{-1}$  approximates  $Q_{Y|X}^{-1}$ ,  $\nabla_y \hat{Q}_{Y|X}^{-1}$  may not necessarily approximate well  $\nabla_y Q_{Y|X}^{-1}$ . Empirically, small errors in the Jacobian can be magnified in  $\det(\cdot)$ , which distorts HPD superlevel sets. As shown in Section 6.1, in our experiments,  $\hat{Q}_{Y|X}$  approximated well the true quantile function. Nonetheless, we found the HDP approach of producing conformal sets empirically suboptimal w.r.t. the volume of the produced set and conditional coverage.

## G IMPORTANCE OF CONVEX POTENTIAL

The fact that the transformation is cyclically monotone is crucial for defining a statistically meaningful notion of multivariate rank. Cyclic monotonicity is the extension of monotonicity in the multidimensional setting. The definition of multivariate ranks is discussed in the pioneering work of Hallin et al. (2021) and in studies by Galichon (2018); Carlier et al. (2016; 2017; 2022); Chernozhukov et al. (2017).

### G.1 CYCLICAL MONOTONICITY

A subset  $S \subseteq \mathbb{R}^d \times \mathbb{R}^d$  is said to be cyclically monotone if, for any finite collection of points  $\{(\mathbf{x}_1, \mathbf{y}_1), \dots, (\mathbf{x}_k, \mathbf{y}_k)\} \subseteq S$ , the following inequality holds:

$$\langle \mathbf{y}_1, \mathbf{x}_2 - \mathbf{x}_1 \rangle + \langle \mathbf{y}_2, \mathbf{x}_3 - \mathbf{x}_2 \rangle + \dots + \langle \mathbf{y}_k, \mathbf{x}_1 - \mathbf{x}_k \rangle \leq 0.$$

A finite subset  $S = \{(\mathbf{x}_1, \mathbf{y}_1), \dots, (\mathbf{x}_n, \mathbf{y}_n)\} \subseteq \mathbb{R}^d \times \mathbb{R}^d$  is cyclically monotone if and only if the inequality above holds for  $k = n$ . Equivalently,  $S$  maximizes the empirical correlation  $\sum_{i=1}^n \langle \mathbf{x}_i, \mathbf{y}_i \rangle$  among all pairings of  $\{\mathbf{x}_1, \dots, \mathbf{x}_n\}$  and  $\{\mathbf{y}_1, \dots, \mathbf{y}_n\}$ , or, equivalently, minimizes the empirical distance  $\sum_{i=1}^n \|\mathbf{y}_i - \mathbf{x}_i\|^2$ . In other words, a finite subset  $S$  is cyclically monotone if and only if the pairs  $(\mathbf{x}_i, \mathbf{y}_i)$  form the solution to the optimal assignment problem with cost  $\|\mathbf{y}_i - \mathbf{x}_i\|^2$ . Rockafellar's Lemma (1966) (Rockafellar, 2015), establishes a relation between cyclical monotonicity and convex functions.

**Theorem 5** (Rockafellar (2015), Theorems 1). *The subdifferential  $\partial\psi$  of a convex function  $\psi$  on  $\mathbb{R}^d$  enjoys cyclical monotonicity. Conversely, any cyclically monotone set  $S$  of  $\mathbb{R}^d \times \mathbb{R}^d$  is contained in the subdifferential  $\partial\psi$  of some convex function  $\psi$  on  $\mathbb{R}^d$ .*

**Theorem 6** (Brenier (1991)). *Let  $\mu$  and  $\nu$  be two probability measures on  $\mathbb{R}^d$ , with  $\mu$  absolutely continuous with respect to the Lebesgue measure. Let  $T: \mathbb{R}^d \rightarrow \mathbb{R}^d$  be a measurable map that pushes forward  $\mu$  onto  $\nu$ , i.e.*

$$T_\# \mu = \nu.$$

*Then, there exists a unique (up to  $\mu$ -almost everywhere equality) cyclically monotone map  $\nabla\varphi: \mathbb{R}^d \rightarrow \mathbb{R}^d$ , where  $\varphi$  is a convex function, such that  $T = \nabla\varphi \circ S$  with  $S: \mathbb{R}^d \rightarrow \mathbb{R}^d$  a measure-preserving map, that is  $S_\# \mu = \nu$ . Moreover,  $\nabla\varphi$  is the optimal transport map pushing  $\mu$  forward to*

1404  $\nu$  for the quadratic cost  $c(x, y) = \frac{1}{2}\|x - y\|^2$ , and it minimizes  $\int_{\mathbb{R}^d} \|T(x) - x\|^2 d\mu(x)$  among all  
 1405 measurable maps satisfying  $T_{\#}\mu = \nu$ .  
 1406

1407 Brenier's theorem states that any measurable transport map  $T$  can be factorized as:

1408 (i) A measure-preserving rearrangement  $S$ , which redistributes mass within  $\mu$  without altering it.  
 1409 (ii) A cyclically-monotone map  $\nabla\varphi$ , which moves  $\mu$  optimally (in the quadratic sense) to  $\nu$ .  
 1410

1411 When defining multivariate quantiles, we learn the cyclically monotone pushforward between the  
 1412 data distribution  $\nu$  over  $\mathbb{R}^d$  and the standard normal Gaussian distribution denoted  $\mu$  (we could take  
 1413 the uniform distribution on the disk or the multivariate normal with 0 mean and identity covariance).  
 1414 We assume that  $\nu$  is absolutely continuous w.r.t. the Lebesgue measure.

1415 Assume that we stake  $MVN(0, I)$ , we obtain the  $(1 - \alpha)$  coverage sets, we take balls of radius  $\rho_\alpha$ ;  
 1416 where  $\rho_\alpha$  is the  $1 - \alpha$  quantile of a  $\chi^2$  distribution with  $d$  degrees of freedom and compute their  
 1417 pre-images under this map.

1418 If we use a transform which is not cyclically monotone, the regions that we will obtain using this  
 1419 method will of course have the correct coverage, but might have wild shapes, because the measure  
 1420 preserving transform (appearing in Brenier's polar factorization) can be arbitrarily complex. Indeed,  
 1421 there infinitely many pushforward map between  $\mu$  and  $\nu$ , but only the cyclically monotone pushfor-  
 1422 ward allows to define a quantile function and the associated ranks and signs that are meaningful.

## 1423 G.2 EXAMPLE OF NON CYCLICALLY-MONOTONE MAP

1424 We illustrate this phenomenon in dimension  $d = 2$ .

1425 Assume that the data distribution  $\nu$  is multivariate normal with a non-singular covariance matrix  $\Gamma$ .  
 1426 We map it to the multivariate distribution with density  $\frac{d\mu}{d\text{Leb}}(u) = MVN(u; 0, I)$ , where  $\text{Leb}$  is the  
 1427 Lebesgue measure.

1428 The cyclically monotone transform is  $\nabla\Phi(u) = \Gamma^{-1/2}u$ , where  $\Gamma^{-1/2}$  is the Hermitian root-square  
 1429 of  $\Gamma$  (and  $\Phi(u) = (1/2)u^\top\Gamma^{-1/2}u$  is a convex function). The Brenier polar factorization theorem  
 1430 shows that any pushforward  $\nu \rightarrow \mu$  can be decomposed as  $T = \nabla\Phi \circ \sigma$ , where  $\sigma$  is a measure-  
 1431 preserving map for  $\mu = N(0, I)$ . This measure preserving maps is not cyclically monotone and  
 1432 therefore might affect the ranks used in the construction.

1433 There are many ways to construct measure preserving maps of  $MVN(0, I)$ . We provide such a  
 1434 construction in  $\mathbb{R}^2$ . Let  $(x(t), y(t))_{t \geq 0}$  a two dimensional random process which evolves according  
 1435 to the the ODE:

$$1436 \dot{x}(t) = v_{t,x}(x(t)), \quad \dot{y}_t = v_{t,y}(y(t)),$$

1437 where  $v_t = (v_{t,x}, v_{t,y})$  is the velocity field. Denote by  $p_t$  the pdf of  $(x(t), y(t))$  at time  $t$ . The  
 1438 continuity equation shows that

$$1439 \nabla_t p_t + \nabla \cdot (p_t v_t) = 0$$

1440 The density is invariant under the flow of the ODE is  $\nabla \cdot (p_t v_t) = 0$  for all  $t \geq 0$ , in which case  
 1441  $p_t = p_0$  for all  $t \geq 0$ . Denote  $w_t = p_t v_t$ . A canonical way to ensure  $\nabla \cdot w_t = 0$  is to set  
 1442  $w_{t,x} = \partial_y \Psi(x, y)$  and  $w_{t,y} = -\partial_x \Psi(x, y)$ , where  $\Psi$  plays the role of an Hamiltonian. If we start  
 1443 from  $p_0$  the pdf of  $MVN(0, I)$ , the flow of the ODE

$$1444 \dot{x}(t) = \frac{1}{p_0}(x(t), y(t))\partial_y \Psi(x(t), y(t)) \quad \dot{y}(t) = -\frac{1}{p_0}(x(t), y(t))\partial_x \Psi(x(t), y(t))$$

1445 is measure preserving for  $p_0$ , for any  $t > 0$ . In other words, if we define  $(x(t), y(t)) = F_{0 \rightarrow t}(x(0), y(0))$  the flow of the solutions of the ODE,  $F_{0 \rightarrow t} \# p_0 = p_0$ . Along the flow of the  
 1446 solutions,

$$1447 \frac{d}{dt} \Psi(x(t), y(t)) = \partial_x \Psi(x(t), y(t)) \dot{x}(t) + \partial_y \Psi(x(t), y(t)) \dot{y}(t) = 0$$

1448 so the Hamiltonian  $\Psi$  is constant along the orbit:  $\Psi(x(t), y(t)) = C$ . We illustrate this with the  
 1449 mixing

$$1450 \Psi(x, y) = (x^2 + y^2)^{3/2}(1 - x^2 - y^2)y$$

1451 Results are presented in Figure 5. In (A., B.), we show the level set obtained by applying the  
 1452 cyclically monotone transform. In (C.,D.) we show the level sets obtained using a non cyclically

1458

1459

1460

1461

1462

1463

1464

1465

1466

1467

1468

1469

1470

1471

1472

1473

1474

1475

1476

1477

1478

1479

1480

1481

1482

1483

1484

1485

Figure 5: Two pushforward operators. (A., B.) Level sets of latent distribution chosen to be standard Gaussian. (B.) Pushforward of level sets by cyclically monotone operator. (D.) Pushforward of level sets by non cyclically operator, generated by flow. (E., F.) Empirical Density Estimates, based on points sampled from cyclically monotone operator (E.) and non cyclically monotone operator (F.).

1490

1491

1492

1493

monotone transformation  $T$ , obtained by integrating the Hamiltonian flow until tile  $t = 1.5$ . (E., F.) show empirical density estimate from  $10^6$  points, sampled from two different operators.

1494

1495

1496

It is clear that a transformation that is not cyclically monotone does not define a notion of ranks similar to the one described in Hallin et al. (2021), and cannot be used to construct a conformalization procedure similar to ours.

1497

1498

1499

## H DETAILED EXPERIMENTAL RESULTS

1500

1501

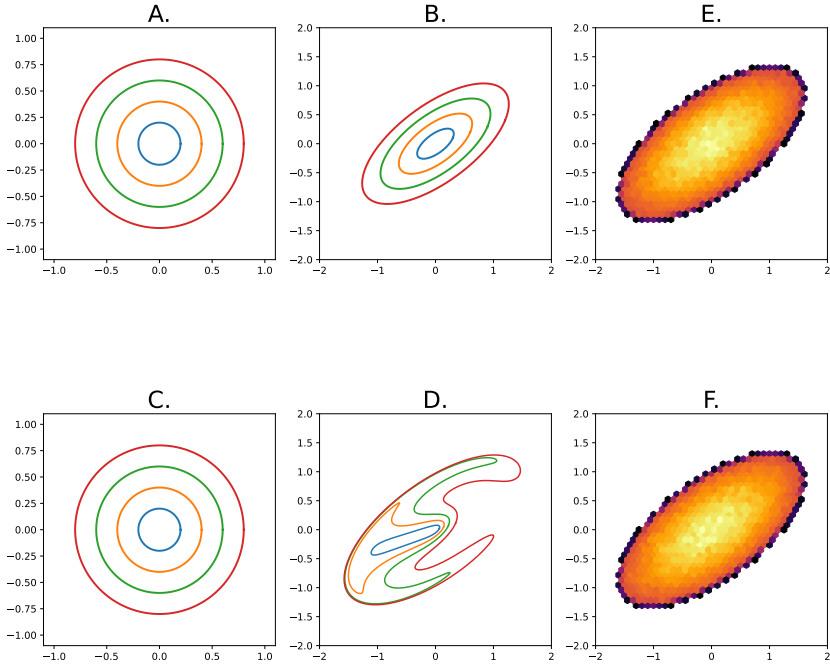
### H.1 OPTIMAL TRANSPORT METRICS

1502

1503

1504

- **Wasserstein distances.** We compute Wasserstein-2 and Sliced Wasserstein distances using the *POT* library Flamary et al. (2021).
- **KDE-L1.** To estimate the  $L^1$  distance between kernel density estimators, we draw 1000 samples from both  $Q_{Y|X}^{-1}$  and its approximation  $\widehat{Q}_{Y|X}^{-1}$ . We then fit Gaussian kernel density estimates to each sample set and report the average pointwise  $L^1$  difference between the two densities, evaluated at points drawn from  $Q_{Y|X}^{-1}$ .
- **KDE-KL.** The Kullback–Leibler divergence is computed following the same procedure as KDE-L1. We report the average pointwise KL divergence between the fitted densities at points drawn from  $Q_{Y|X}^{-1}$ .



1512 • **L2-UV.** To compute the unexplained variance ratio, we sample  $n_u$  points from  $u_{\text{test}} \sim F_U$   
 1513 and  $n_x$  points from  $x_{\text{test}} \sim F_X$ . The L2-UV distance is then defined as  
 1514

$$1515 \frac{1}{n_x + n_u} \sum_{x_{\text{test}}, u_{\text{test}}} \frac{\|Q_{U|X}(u_{\text{test}}, x_{\text{test}}) - \hat{Q}_{U|X}(u_{\text{test}}, x_{\text{test}})\|_2}{\left\| \frac{1}{n_u} \sum_{u_{\text{test}}} Q_{U|X}(u_{\text{test}}, x_{\text{test}}) - Q_{U|X}(u_{\text{test}}, x_{\text{test}}) \right\|_2}.$$

1518 **H.2 OPTIMAL TRANSPORT EXPERIMENTS DATASETS**

1519 **Banana Dataset.** This dataset is largely used in vector quantile estimation for testing the non-  
 1520 linearity of estimators. It was introduced in (Feldman et al., 2023) and used in (Carlier et al., 2017;  
 1521 Rosenberg et al., 2023). It represents a banana-shaped random variable in  $\mathbb{R}^2$ , changing its position  
 1522 and skewness based on latent random variable from  $\mathbb{R}^1$ . Data generative process can be described  
 1523 as:  
 1524

$$1525 X \sim \mathcal{U}[0.8, 3.2], \quad Z \sim \mathcal{U}[-\pi, \pi], \quad \varphi \sim \mathcal{U}[0, 2\pi], \quad r \sim \mathcal{U}[-0.1, 0.1],$$

$$1526 \hat{\beta} \sim \mathcal{U}[0, 1]^k, \quad \beta = \frac{\hat{\beta}}{\|\hat{\beta}\|_1},$$

$$1527 Y_0 = \frac{1}{2}(-\cos(Z) + 1) + r \sin(\varphi) + \sin(X),$$

$$1528 Y_1 = \frac{Z}{\beta X} + r \cos(\varphi),$$

$$1529 \mathbf{X} = X, \mathbf{Y} = \begin{bmatrix} Y_0 \\ Y_1 \end{bmatrix}.$$

1536 We take  $\mathbf{X}$  as and  $\mathbf{Y}$  as observed random variables.

1537 Full set of metrics for Banana dataset is accessible at fig. 7. Metrics for convex potential, that was  
 1538 trained on Banana dataset can be found at fig. 8.

1539 **Rotating Star.** This dataset is inspired by (Rosenberg et al., 2023) rotating star example. Observed  
 1540 random variable represents a three point star in  $\mathbb{R}^2$  that rotates based on latent variable from  $\mathbb{R}$ . Data  
 1541 generative process can be described as:  
 1542

$$1543 (u_0, u_1) \sim \mathcal{N}(0, I), \quad X \sim \mathcal{U}\left[0, \frac{2}{3}\right],$$

$$1544 \theta = \arctan\left(\frac{u_1}{u_0}\right), \quad s(\theta) = 1 + 3 \cos(3\theta),$$

$$1545 \mathbf{R}(\varphi) = \begin{bmatrix} \cos \varphi & -\sin \varphi \\ \sin \varphi & \cos \varphi \end{bmatrix},$$

$$1546 \mathbf{Y} = \mathbf{R}(\varphi)(s(\theta)u_0, s(\theta)u_1)^\top, \mathbf{X} = X,$$

1547 where  $\varphi$  is a rotation angle. We take  $\mathbf{X}$ ,  $\mathbf{Y}$  as observed variables.

1548 Full set of metrics for Star dataset is accessible at Figure 9. Metrics for convex potential, that was  
 1549 trained on Star dataset can be found at Figure 10

1550 **Glasses.** This dataset is introduced in (Brando et al., 2022). It represents two modal distribution,  
 1551 where random variable is in  $\mathbb{R}$ . With  $X \sim \mathcal{U}[0, 1]$ , data generative process can be described as:  
 1552

$$1553 z_1 = 3\pi X, \quad z_2 = \pi(1 + 3X), \quad \epsilon \sim \text{Beta}(\alpha = 0.5, \beta = 1),$$

$$1554 Y_1 = 5 \sin(z_1) + 2.5 + \epsilon, \quad Y_2 = 5 \sin(z_2) + 2.5 - \epsilon,$$

$$1555 \gamma \sim \text{Categorical}(0, 1),$$

$$1556 \mathbf{Y} = (1 - \gamma)Y_1 + \gamma Y_2.$$

1557 We take  $\mathbf{X}$ ,  $\mathbf{Y}$  as observed variables. Full set of metrics for Glasses dataset is accessible at Figure 11.  
 1558 Metrics for convex potential, that was trained on Glasses dataset can be found at Figure 12

1566 **Neal’s funnel distribution.** The classical funnel distribution (Neal, 2003) is defined on  $\mathbb{R}^{d+1}$  as  
 1567

$$1568 \quad v \sim \mathcal{N}(0, \sigma^2), \quad x_i | v \sim \mathcal{N}(0, \exp(v)), \quad i = 1, \dots, d,$$

1569 so that the joint density of  $(v, x_1, \dots, x_d)$  is  
 1570

$$1571 \quad p(v, x) = \frac{1}{\sqrt{2\pi\sigma^2}} \exp\left(-\frac{v^2}{2\sigma^2}\right) \prod_{i=1}^d \frac{1}{\sqrt{2\pi e^v}} \exp\left(-\frac{x_i^2}{2e^v}\right).$$

1574 For large negative values of  $v$ , the conditional variance of the  $x_i$ ’s shrinks, yielding a narrow region  
 1575 (the “neck” of the funnel), whereas large positive  $v$  produces very diffuse  $x_i$ ’s (the “mouth”). This  
 1576 strong nonlinearity makes the distribution challenging for MCMC methods.  
 1577

1578 **Multidimensional funnel.** A natural generalization introduces a  $k$ -dimensional scale vector  $v =$   
 1579  $(v_1, \dots, v_k)$  with

$$1580 \quad v_j \sim \mathcal{N}(0, \sigma^2), \quad x_{j,\ell} | v_j \sim \mathcal{N}(0, \exp(v_j)), \quad \ell = 1, \dots, m,$$

1582 so that each  $v_j$  controls a block of  $m$  Gaussian variables. The joint distribution then lives in di-  
 1583 mension  $k(1 + m)$  and exhibits multiple funnel directions simultaneously. This high-dimensional  
 1584 geometry is frequently used as a stress test for MCMC and normalizing flow methods.  
 1585

### 1586 H.3 DETAILED RESULTS OF THE CONFORMAL PREDICTION EXPERIMENTS

1587 We present more detailed results on conditional coverage on real datasets, involving more variations  
 1588 of our methods and more nominal levels  $\alpha$ .  
 1589

1590 **Methods.** We include the HPD variant of our method as well as models estimating either the  
 1591 forward (U) or the inverse (Y) quantile map.  
 1592

1593 For methods labeled with Y, we model the function  $\psi$  with a neural network and have  $\widehat{Q}_{Y|X}^{-1}(y, x) =$   
 1594  $\nabla_y \psi(y, x)$ . For methods labeled with U we model function  $\varphi$  and get  $\widehat{Q}_{Y|X}(y, x) = \nabla_u \varphi(u, x)$ .  
 1595

1596 Method Quantile corresponds to using the Monge-Kantorovich rank to construct the predictive re-  
 1597 gions, assuming that we have found exactly the mapping to the reference standard multidimensional  
 1598 normal distribution. In this particular case, the squared ranks follow the Chi-square distribution  
 1599 and the corresponding radius for the construction of the pullback-type prediction set can be found  
 1600 exactly.  
 1601

1602 The methods labeled with RF correspond to fitting our model to the residuals of  $s = y - \hat{f}(x)$  of a  
 1603 base Random Forest predictor  $\hat{f}$ . Base predictor uses 25% of the training data and remainder is used  
 1604 to train our model.  
 1605

1606 **Implementation details.** For baseline methods we use the original authors implementation, where  
 1607 available and their suggested values for hyperparameters. For our methods, we select the number  
 1608 of parameters for neural networks to be roughly 10% of the number of training samples. We tune  
 1609 the other hyperparameters for each dataset using a separate data split and utilize the mean coverage  
 1610 error of the pullback sets at different levels of  $\alpha$  as a performance measure. All experiments were  
 1611 replicated using 10 random splits of the data into training, calibration, and test parts.  
 1612

1613 **Discussion.** The Quantile method fails to achieve the nominal levels of conditional coverage,  
 1614 which suggests that a supporting measure like conformal prediction is indeed required. Unfortu-  
 1615 nately, HPD approaches do not perform well on many occasions, proving that density estimation in  
 1616 multiple dimensions is still a difficult to solve problem.  
 1617

1618 Using a base model and fitting quantile regression to the residuals instead of directly  $Y$  provides less  
 1619 variable results, but does not always improve performance of our methods.  
 1620

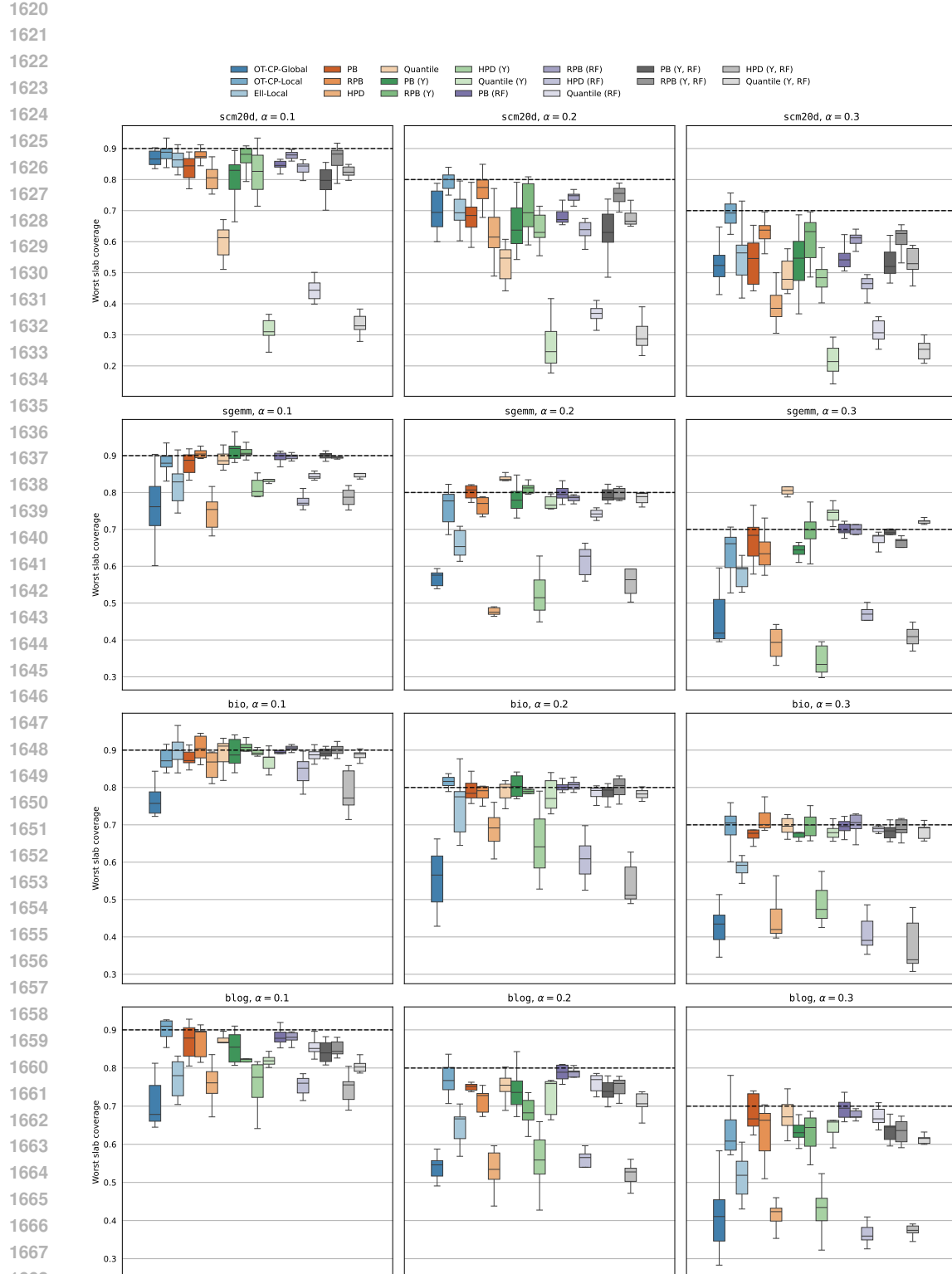


Figure 6: Worst slab coverage at different nominal miscoverage  $\alpha$  levels for conformal prediction methods, achieved on large datasets.

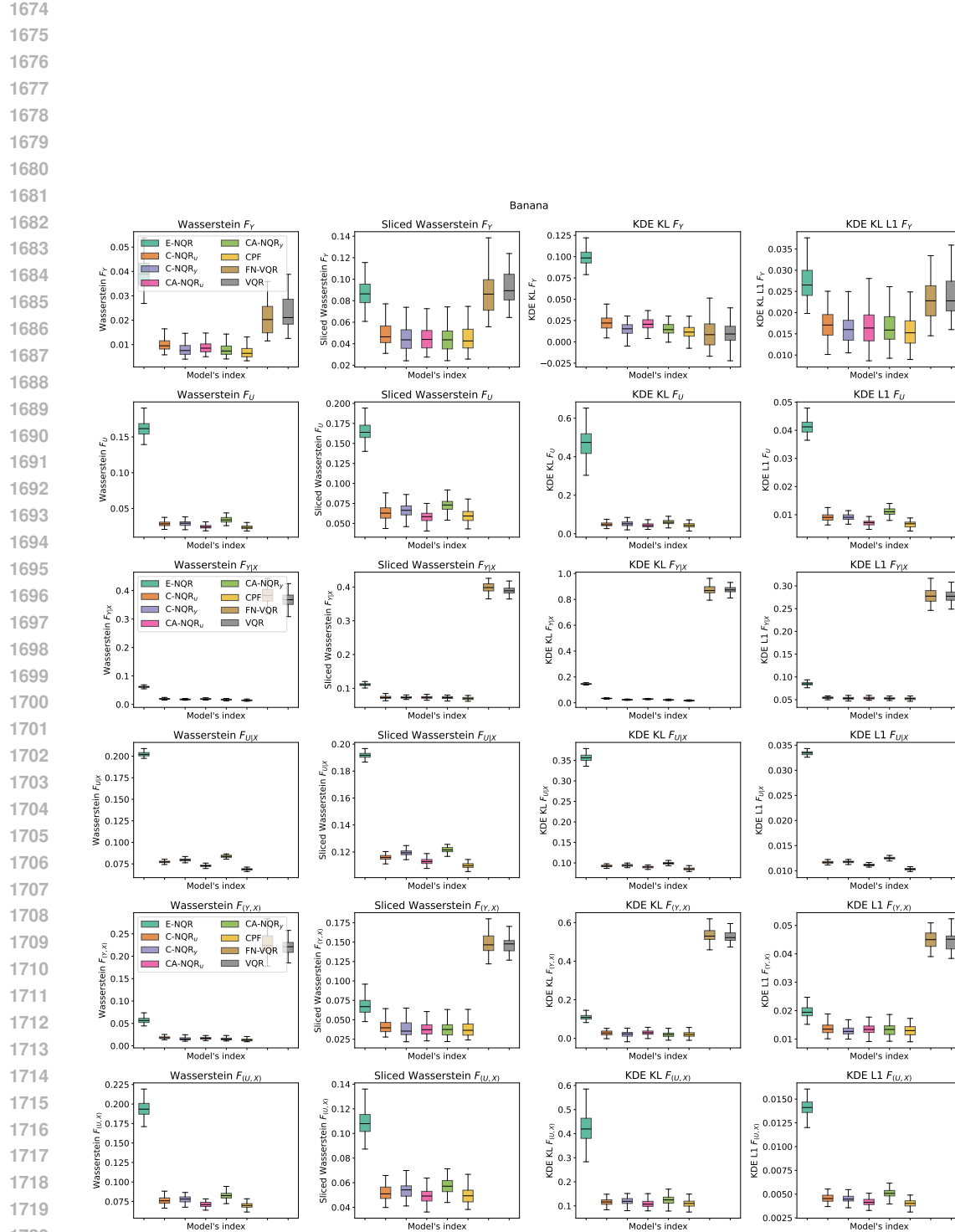


Figure 7: Full set of metrics for Banana dataset.

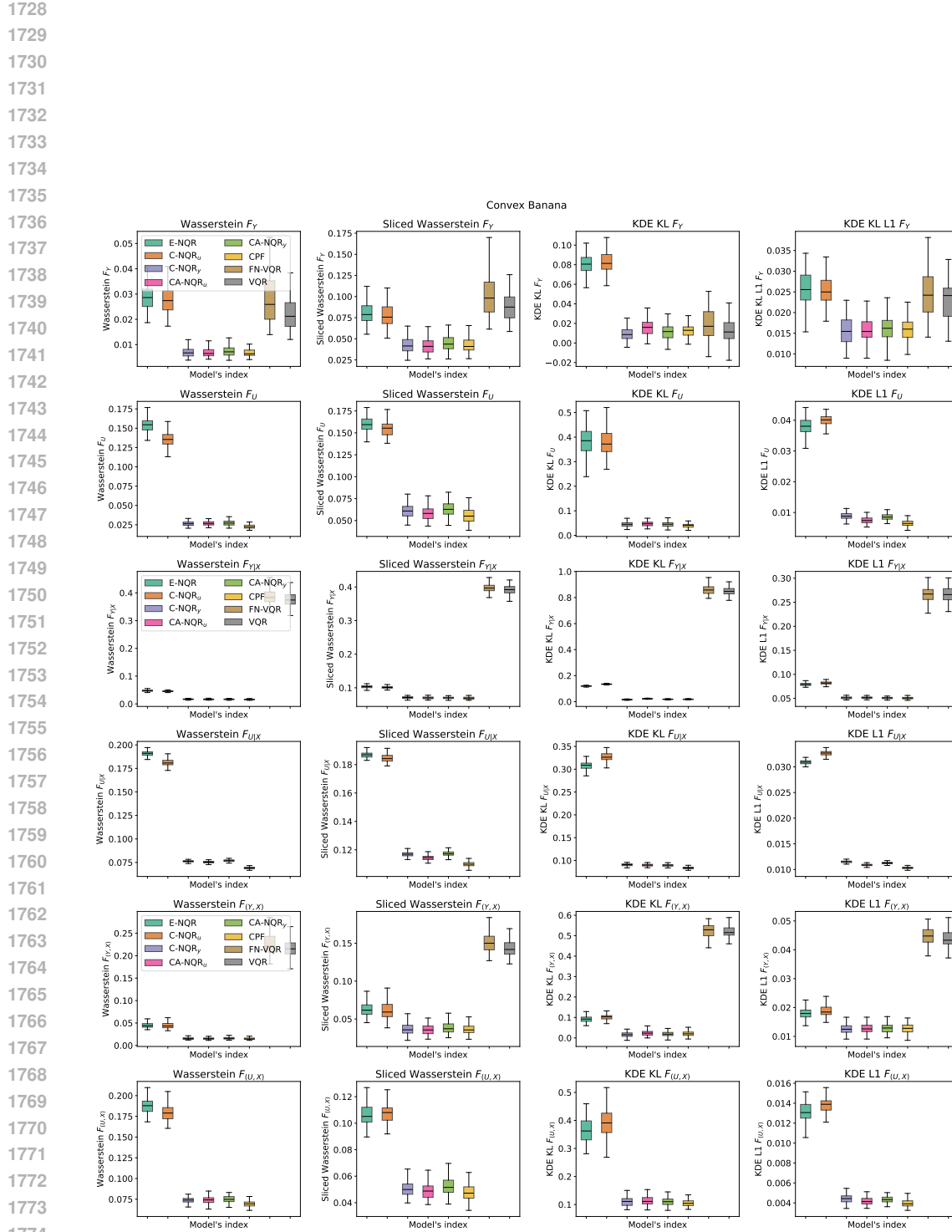


Figure 8: Full set of metrics for Banana dataset.

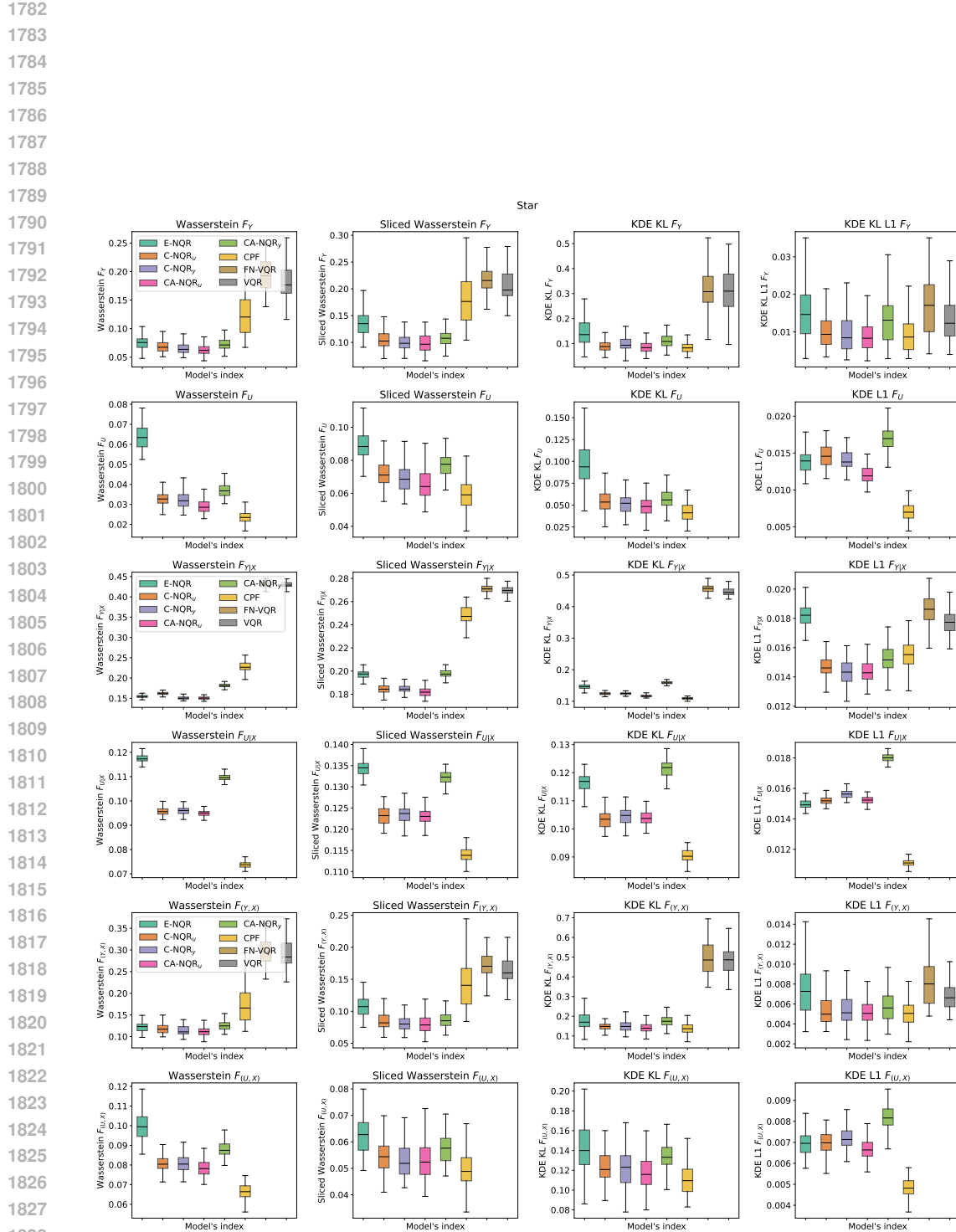


Figure 9: Full set of metrics for Star dataset.

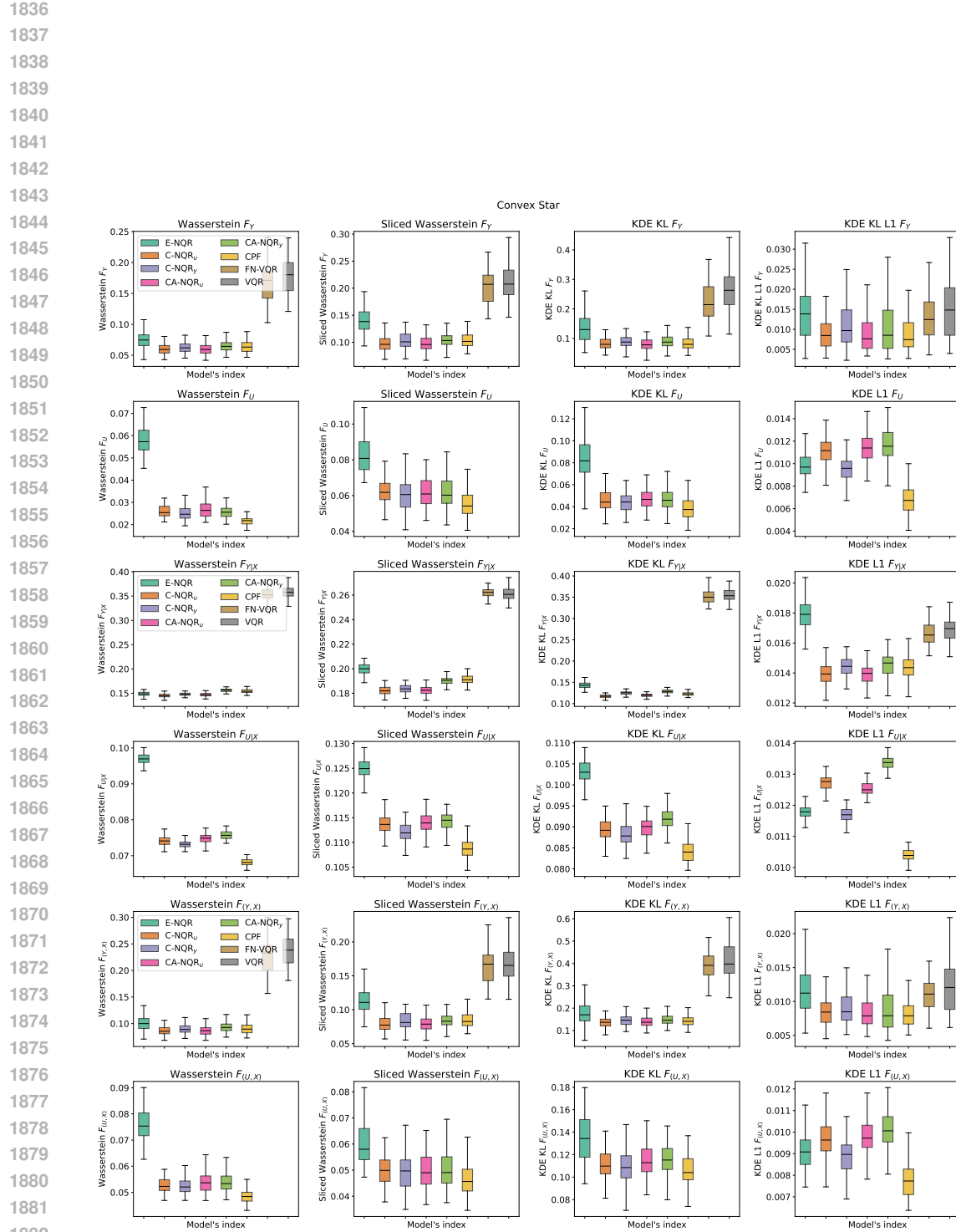


Figure 10: Full set of metrics for Convex Star dataset.

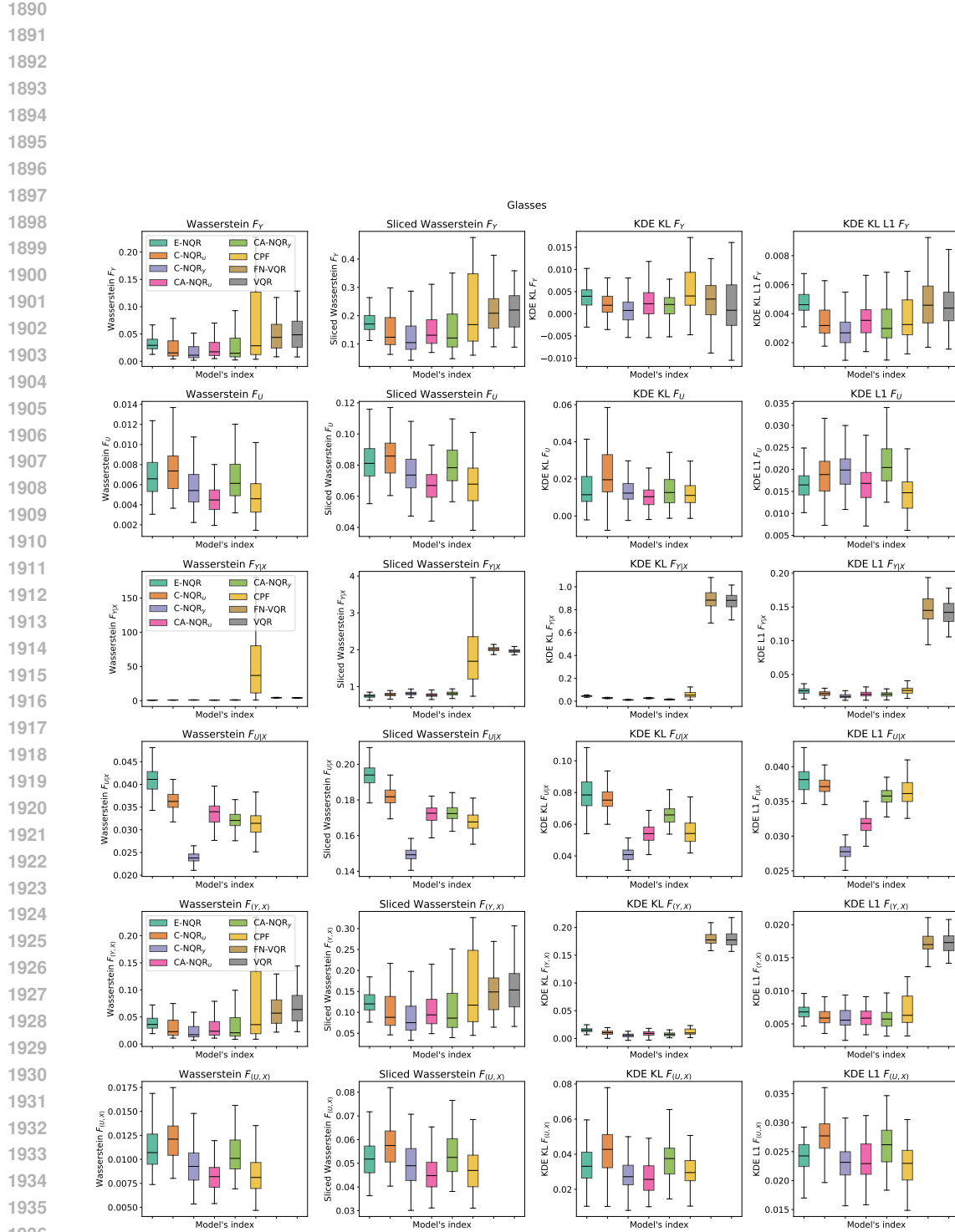


Figure 11: Full set of metrics for Glasses dataset.

